Available online at www.sciencedirect.com
SCIENCE DIRECT®
Journal of Computational Physics 210 (2005) 133–170
JOURNAL OF COMPUTATIONAL PHYSICS
www.elsevier.com/locate/jcp

A new category of Hermitian upwind schemes for computational acoustics

G. Capdeville *

Laboratoire de Mécanique des fluides, Ecole Centrale de Nantes, 1, rue de la Noë, B.P. 92101, 44321 Nantes Cedex 3, France

Received 9 July 2004; received in revised form 4 April 2005; accepted 7 April 2005
Available online 23 May 2005

Abstract

A new high-order upwind scheme is developed to solve linear acoustics. In order to produce a compact scheme with a high level of precision, a Hermite interpolation is used. An algorithm in three stages is built in order to optimize the procedure of discretization. In the "reconstruction stage", a local spatial interpolator based on an upwind stencil is defined. In the "decomposition stage", the calculation of a wave model adapted to the decomposition of the time-derivatives in simple wave contributions is derived; then the local spatial interpolator is used in order to calculate the wave strengths for each wave. In the "evolution stage", we update by means of a procedure similar to that of Cauchy–Kovaleskaya, the discrete variable and its derivatives, by using the information brought by each simple wave. Specific boundary conditions are finally established. In this way, a third-order upwind Hermitian scheme may be constructed ("Δ-P3 scheme"). A one-dimensional analysis in Fourier series shows the principal properties of such a scheme. The effectiveness and the exactitude of the new compact scheme are shown by their applications to several two-dimensional problems and by comparisons to competing finite difference method for wave propagation.

Keywords: Hermitian schemes; Upwind discretization; Wave-modelling; Acoustics; Upwind boundary conditions

1. Introduction

Computational acoustics is a recent tool to deal with acoustic problems. Since the acoustic waves are isotropic, non-dispersive and non-dissipative in their propagation, numerical schemes, which take into account these characteristics, are desirable. In this respect, it appears that specific high-order schemes are adapted better for computational acoustics than the current computational fluid dynamics (CFD) schemes,

* Tel.: +33 2 4037 1651; fax: +33 2 4037 2523.
E-mail address: guy.capdeville@ec-nantes.fr.

0021-9991/$ - see front matter © 2005 Elsevier Inc. All rights reserved.
doi:10.1016/j.jcp.2005.04.005

since the latter are usually dispersive, anisotropic and even strongly dissipative. The feasibility of such computations is mainly dictated by the number of grid points that must be employed to solve each wavelength without incurring an unacceptable error. Usually, conventional methods of CFD need values around 30 points-per-wavelength to obtain a total dissipation error below 15%, while the powerful numerical algorithms require only 8 points per wavelength.

Broadly speaking, there are two traditional ways to conceive methods with high resolution for acoustic problems. The first approach privileges spatially centred computational stencils; the second implies the use of spatially upwinded stencils.

Among what one call "centred schemes", the explicit DRP scheme [11] is usually employed. Essentially, the idea is to optimize the coefficients of the scheme, in the wave number and frequency space, in order to solve with a high resolution, the waves having wavelengths longer than $4\Delta x$. In this way, are produced finite-difference schemes that have relations of dispersion as close as possible to the original partial differential equations. This idea to optimize the scheme coefficients in order to minimize a specific type of error was employed successfully during these last years by many researchers [6,12–15]. All these schemes share a centred discrete stencil to approach the first derivatives: they, therefore, are intrinsically non-dissipative. Although non-dissipative schemes are ideal for acoustics, numerical dissipation is still necessary to deaden any non-physical wave ("spurious wave") generated by boundary and/or inadequate initial conditions. Spurious waves can be excited by rapid grid stretching and changes in the differencing scheme (e.g. across a multi-block interface or at a computational boundary). Generally, high-order dissipation terms are added in order to remove spurious oscillations. However, the quantity of artificial dissipation required depends on the problem considered. To cure these problems, upwind schemes can be used. Upwind schemes are intrinsically dissipative; therefore, they are, in theory, able to remove spurious oscillations without adding an additional term of damping. Moreover, the use of an upwind-biased stencil based on a local direction of propagation of wave, makes it possible to treat the boundaries more effectively, by distinguishing waves entering and outgoing from the computational domain. Upwind DRP schemes [20], upwind Leap-Frog schemes [8,17], the method of space–time conservation element and solution element [18], optimized WENO schemes [16], or the Discontinuous Galerkin (DG) method [19] are all viable solutions.

The goal of this paper is twofold: initially, we wish to present a method based on a multi-dimensional upwind-biased stencil in order to develop strongly accurate algorithms for computational linear acoustics; in the second place, we wish to incorporate non-reflective boundary conditions without resorting to non-physical arguments.

In order to achieve this goal, the problem is broken up into three sub-problems, namely:

- a "reconstruction stage"
- a "decomposition stage"
- an "evolution stage"

In the stage of reconstruction, we employ the concept of "local spatial interpolator" in order to produce a polynomial of a compact high nature, approaching the solution on a given discrete cell. For this purpose, we define the function and its derivatives as numerical data to calculate the coefficients of the polynomials.

The important advantage of a Hermite interpolation is the compactness of the basis stencil. This idea is not new. Since Van-Leer's schemes [21] until Hermite WENO schemes [22] or Chang's method [18], there exist much of attempts in the literature to conceive schemes using a narrower stencil by actualization of more than one degree of freedom per discrete point. More specifically, Goodrich's approach [23,24] is closely related to acoustic problems: Hermitian interpolation is defined on central stencils that are in oneself unstable. Staggered spatial grids are then employed in order to maintain the stability of the resulting scheme [24]: because of its upwind-biased nature, the solution that we propose does not need to use staggered spatial grids and makes it possible to preserve space compactness.

The stage of decomposition is based on the ideas suggested by Roe [4] a few years ago. In order to construct "truly multi-dimensional" schemes for the non-linear steady Euler equations, Roe suggested model flows, composed of elementary solutions of the multi-dimensional unsteady equations. Our point of view is slightly different. Indeed, the problem that we consider is linear (acoustics) and unsteady (propagation of waves).

To our knowledge, the only attempt to model linear wave propagation by breaking up the time-derivatives into simple wave contributions, was the speculative study carried out by Roe [3]. In this study, however, the wave directions remain associated with the gradients in the data: although the problem is linear, the discrete scheme has as a harmful consequence to generate a nonlinear method with the possible appearance of nonlinear instabilities. In order to draw aside this difficulty and based upon omni-directional wave propagation for acoustics, we impose the directions of propagation arbitrarily, independently of the local data or the grid directions. With this approximation, the resulting discrete model remains linear and produces a multi-dimensional decomposition of the time-derivatives.

To finish, the stage of evolution employs a procedure of Cauchy–Kovaleskaya [1] in order to update the solution and its derivatives. This process makes it possible to associate a temporal "fluctuation" (or disturbance) of a high nature with each simple wave; each fluctuation is then distributed again to the vertices of the discrete stencil, providing the changes used in order to update the solution and its derivatives.

This method simultaneously approaches the derivative space and temporal. Thus, no intermediate semi-discrete form is produced and the numerical scheme is put in a more compact form. This process in three stages of discretization provides a modular method whose each stage can be optimized distinctly. It is an advantage, since the algorithm becomes more flexible then and can be adapted to deal with distinct linear hyperbolic problems. In this way, we can develop high-order and compact upwind schemes for linear acoustics.

Moreover, this approach supports the effective numerical handling of boundary conditions. Indeed, it is well known that high-order finite-difference schemes tolerate short wavelength spurious numerical waves. These spurious waves are often produced at computational boundaries (internal and external) and deteriorate the numerical solution. When an excessive quantity of spurious waves is produced, this leads not only to the degradation of the numerical solution but also, in much of case, to numerical instability. To obtain a numerical solution of high quality, there is thus a need to destroy the spurious numerical waves with short wavelength. This can be done by artificial damping terms.

As previously indicated, an important characteristic of an upwind scheme is automatically to add artificial dissipation without need for adjusting the coefficients of the damping terms. This characteristic is shared by the procedures that we chose and makes easier the numerical treatment of the radiation boundary conditions that exist in acoustics.

While putting at the zero only fluctuations brought by the waves of entry to a given boundary, there is no need to modify neither the equations nor the algorithm at the boundary points. It is the advantage of using an upwind method, which clearly identifies waves entering and outgoing the computational domain.

The organization of this paper is as follows: Section 2 presents the basic scheme for unidimensional scalar advection. We develop a third-order version (the "Δ-P3 scheme") with, like unknowns, the primitive variables and its first space-derivatives. We employ a Fourier analysis then in order to calculate the errors of dissipation and dispersion. Then, we provide numerical examples to compare the behaviour of the Δ-P3 scheme with the well-known DRP scheme of Tam and Webb. In Section 3, we extend the process to two-dimensional linear acoustics. In a reconstruction stage, the shape of the spatial interpolator is initially defined and then the wave-model is presented in the decomposition stage. Then, the evolution stage is detailed in order to obtain the algebraical expressions which characterize the Δ-P3 scheme. The boundary conditions are then derived: the radiation and wall boundary conditions are formulated in order to produce non-reflective conditions. Section 4 presents the analysis of the scheme resulting by using analytic solutions like references and by comparison with the DRP scheme. In order to validate the boundary conditions and to

examine the wave-models, of the applications to several benchmark problems in 2-D, are made. To finish, we present a summary and general conclusions in Section 5. The concept of "spurious component" in the numerical solution is described in Appendix A.

2. Third-order upwind Hermitian schemes: one-dimensional case

We consider the linear advection equation:

$$u_t + au_x = 0 \quad (a \equiv Cte > 0). \tag{1}$$

We define a uniform grid with mesh size $\Delta x \equiv x_{i+1} - x_i$ and time step size $\Delta t \equiv t_{n+1} - t_n$. We then define the CFL (Courant number), subsequently noted v, by the following formula: $v \equiv a\frac{\Delta t}{\Delta x}$. The problem being linear, every derivative of u remains solution of the advection operator. Initially, we describe the construction of the Δ-P3 scheme.

2.1. The "Δ-P3 scheme"

On each grid point, x_i, and for each time, $t_n \equiv n\Delta t$, we define u_i^n as the numerical approximation to the exact point value, $u(x_i, t_n)$. Similarly, the discrete value, r_i^n, will be considered as the numerical approximation of $r(x_i, t_n) \equiv \Delta x \times u_x(x_i, t_n)$. In order to generate an upwind algorithm, let the discrete stencil of the method be defined by the cell $[i-1, i]$. With the previous definitions, this cell possesses four discrete unknowns (Fig. 1). Let us consider the following cubic polynomial which interpolates the numerical data on this cell at the time $t = t_n$:

$$\tilde{u}(x) \equiv c_1 + c_2(x - x_i) + c_3(x - x_i)^2 + c_4(x - x_i)^3. \tag{2}$$

The expansion coefficients, $\{c_i\}_{i=1,2,3,4}$, are obtained from the known data on the grid, by the following relations:

$$\begin{cases} \tilde{u}(x_j) \equiv u_j^n \\ \Delta x \times \tilde{u}_x(x_j) \equiv r_j^n \end{cases} \quad \text{for } j \in \{i-1, i\}. \tag{3}$$

These relations generate a linear system of four equations for the four unknowns $\{c_i\}_{i=1,2,3,4}$. This system is easily inverted to obtain

$$\begin{cases} c_1 = u_i^n, \\ c_2 = \dfrac{r_i^n}{\Delta x}, \\ c_3 = \dfrac{3(u_{i-1}^n - u_i^n) + 2r_i^n + r_{i-1}^n}{\Delta x^2} \approx \dfrac{1}{2}u_{xx}|_i^n, \\ c_4 = \dfrac{2(u_{i-1}^n - u_i^n) + r_i^n + r_{i-1}^n}{\Delta x^3} \approx \dfrac{1}{6}u_{3x}|_i^n. \end{cases}$$

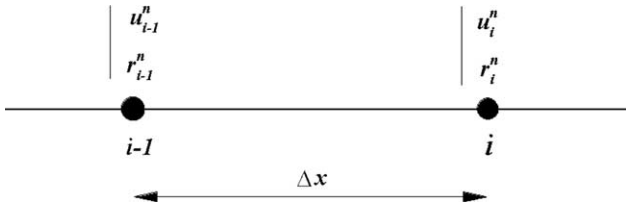

Fig. 1. Δ-P3 scheme: the discrete unknowns on the cell $[i-1, i]$ for $u_t + au_x = 0$.

Then, we expand in Taylor series $u(x_i, t_n + \Delta t)$ and $r(x_i, t_n + \Delta t)$ around the basis point (x_i, t_n):

$$\begin{cases} u(x_i, t_n + \Delta t) = u(x_i, t_n) + \Delta t \times u_t(x_i, t_n) + \frac{\Delta t^2}{2} u_{tt}|_i^n + \frac{\Delta t^3}{6} u_{3t}|_i^n + \mathrm{O}(\Delta t^4), \\ r(x_i, t_n + \Delta t) = r(x_i, t_n) + \Delta t \times r_t(x_i, t_n) + \frac{\Delta t^2}{2} r_{tt}|_i^n + \mathrm{O}(\Delta t^3). \end{cases}$$

We substitute the temporal derivatives by their spatial equivalents, by applying the method used in the proof of the Cauchy–Kovaleskaya theorem [1]:

$$u(x_i, t_n + \Delta t) = u(x_i, t_n) + \Delta t \times \underbrace{u_t(x_i, t_n)}_{=-au_x} + \frac{\Delta t^2}{2} \underbrace{u_{tt}|_i^n}_{=a^2 u_{xx}} + \frac{\Delta t^3}{6} \underbrace{u_{3t}|_i^n}_{=-a^3 u_{3x}} + \mathrm{O}(\Delta t^4),$$

$$r(x_i, t_n + \Delta t) = r(x_i, t_n) + \Delta t \times \underbrace{r_t(x_i, t_n)}_{=-ar_x} + \frac{\Delta t^2}{2} \underbrace{r_{tt}|_i^n}_{=a^2 r_{xx}} + \mathrm{O}(\Delta t^3).$$

Lastly, we truncate the previous series and approximate the spatial derivatives by using the local interpolator, $\tilde{u}(x)(\tilde{r}(x) \equiv \Delta x \times \tilde{u}_x(x))$:

$$\begin{cases} u_i^{n+1} = u_i^n - a\Delta t \times \tilde{u}_x|_i^n + \frac{a^2 \Delta t^2}{2} \tilde{u}_{xx}|_i^n - \frac{a^3 \Delta t^3}{6} \tilde{u}_{3x}|_i^n, \\ r_i^{n+1} = r_i^n - a\Delta t \times \tilde{r}_x|_i^n + \frac{a^2 \Delta t^2}{2} |\tilde{r}_{xx}|_i^n. \end{cases} \tag{4}$$

More explicitly, by developing $\tilde{u}(x)$ and $\tilde{r}(x)$:

$$\begin{cases} u_i^{n+1} = (v-1)^2(2v+1)u_i^n + v^2(3-2v)u_{i-1}^n + v^2(1-v)r_{i-1}^n - v(v-1)^2 r_i^n, \\ r_i^{n+1} = 6v(1-v)(u_i^n - u_{i-1}^n) + (v-1)(3v-1)r_i^n + v(3v-2)r_{i-1}^n. \end{cases} \tag{5}$$

This algebraical formula defines the "Δ-P3 scheme", discretizing (1). Hence, we have generated a third-order upwind and compact scheme. This algorithm is equivalent to the solution by the method of characteristics for (1). However, the Cauchy–Kovaleskaya process produces algorithms that are more general than the method of characteristics. In two or more space dimensions, this process produces algorithms for the linearized Euler equations, which correctly incorporate propagation along characteristic surfaces for the local spatial interpolator taken as the initial data: this is because the equations for the system are directly used to derive the propagator for the local data interpolator.

The Cauchy–Kovaleskaya process results in a family of algorithms with members that have properties which depend on the choice of the spatial interpolator. Algorithms of this type are explicit methods with the same order-of-accuracy in both space and time. In such a case, the order-of-accuracy is the order of the multi-dimensional spatial interpolation.

2.2. Scheme analysis

In order to study the stability and accuracy of the Δ-P3 scheme, let us use a Fourier analysis. For this purpose, we decompose the discrete solution $U_i^n \equiv [u_i^n, r_i^n]^t$, in Fourier series. The solution vector is then assumed to take the following form:

$$U_i^n = \hat{U}(t_n) \times \mathrm{e}^{\mathrm{j}kx_i} \quad (\mathrm{j}^2 = -1,\ k\text{: wave number}).$$

By substituting the above relation into (5), we get the following relation:

$$\hat{U}(t_{n+1}) = G(\beta, v) \times \hat{U}(t_n) \quad (\beta \equiv k \times \Delta x\text{: phase angle})$$

with

$$G(\beta,\nu)\equiv\begin{bmatrix}-\nu^2(3-2\nu)\mathrm{e}^{-\mathrm{j}\beta}-(\nu-1)^2(2\nu+1) & \nu(\nu-1)^2-\nu^2(1-\nu)\mathrm{e}^{-\mathrm{j}\beta}\\ 6\nu(1-\nu)\mathrm{e}^{-\mathrm{j}\beta}-6\nu(1-\nu) & -\nu(3\nu-2)\mathrm{e}^{-\mathrm{j}\beta}-(\nu-1)(3\nu-1)\end{bmatrix}.$$

The complex "amplification matrix" , $G(\beta,\nu)$, possesses two distinct eigenvalues. The first eigenvalue, noted $\lambda_1(\beta,\nu)$, will be defined as the "accurate eigenvalue" since it is associated with the mode that models linear advection with sufficient accuracy. More explicitly, $\lambda_1(\beta,\nu)$ will approximate $\mathrm{e}^{-\mathrm{j}\nu\beta}$, the amplification factor of the exact solution of (1). The remaining eigenvalue, $\lambda_2(\beta,\nu)$, which has no equivalent in the differential problem, will be referred to as the "spurious eigenvalue" (see [2,21] for more details). This spurious eigenvalue is associated with a spurious component in the discrete solution, given by the relation (see Appendix A, for a detailed explanation):

$$\underbrace{\hat{U}(t_{n+1})}_{\substack{\text{num. sol.}\\ \text{at } t=t_{n+1}}}=\underbrace{\lambda_1\times\hat{U}_1(t_n)}_{\text{accurate sol.}}+\underbrace{\lambda_2\times\hat{U}_2(t_n)}_{\text{spurious sol.}}. \tag{6}$$

The accurate component is advected with third-order accuracy; the spurious component is advected with less accuracy: the hope is that this component is heavily damped.

Let us consider the accurate component. If we assume that the truncation error, $\tau(x,t)$, for the Δ-P3 scheme, takes the following form:

$$\tau(x,t)=\alpha\frac{\Delta x^4}{\Delta t}\times\frac{\partial^4 u}{\partial x^4}+\text{following terms}. \tag{7}$$

Then, by using a Fourier transform and the general definition of the truncation error, the following relation can be easily demonstrated:

$$\left[\lambda_1(\beta,\nu)-\mathrm{e}^{-\mathrm{j}\nu\beta}\right]\underset{\beta\to0}{\propto}\alpha\times(\mathrm{j}\beta)^4. \tag{8}$$

Now, let us formulate the eigenvalues for the Δ-P3 scheme that discretizes (1). We obtain the following result:

$$\lambda_{1,2}(\beta,\nu)=(\nu-1)(\nu^2+\nu-1)+\nu\mathrm{e}^{-\mathrm{j}\beta}(3\nu-\nu^2-1)\pm\nu\sqrt{D}$$
$$\text{with } D\equiv[\mathrm{e}^{-2\mathrm{j}\beta}(\nu-1)^2(\nu^2-4\nu+1)+\mathrm{e}^{-\mathrm{j}\beta}(-2\nu^4+6\nu^3+4\nu^2-18\nu+1)+\nu^4-5\nu^3-2].$$

By using the Maple symbolic mathematical computer package, we can demonstrate that the two eigenvalues satisfy the relation identified in [21]:

$$\lambda_{1,2}(\beta,1-\nu)=\mathrm{e}^{-\mathrm{j}\beta}\times\bar{\lambda}_{1,2}(\beta,\nu)\quad\forall\beta. \tag{9}$$

In this relation, the bar denotes the complex conjugate. This property is evidently verified by the exact amplification factor, $\mathrm{e}^{-\mathrm{j}\nu\beta}$. The relation (9) is strictly equivalent to the pair of relations:

$$\begin{cases}|\lambda_{1,2}(1-\nu)|=|\lambda_{1,2}(\nu)|\\ \mathrm{Arg}(\lambda_{1,2}(1-\nu))+\beta=-\mathrm{Arg}(\lambda_{1,2}(\nu))\end{cases}\quad\forall\beta. \tag{10}$$

The first equation implies that $|\lambda_1(\nu)|$ has an extremum for $\nu=1/2$; this extremum is in fact a minimum. Hence, the dissipative error per time step (or amplitude error), $D(\beta,\nu)\equiv1-|\lambda_1(\beta,\nu)|$, has a maximum for this value. On the other hand, the second equation in (10) shows that the phase error per time step, $E(\beta,\nu)\equiv\frac{\mathrm{Arg}(\lambda_1(\beta,\nu))}{\nu\beta}-1$, goes through zero for $\nu=1/2$, regardless of the value of β. Consequently, it will be more practical to confine us to calculate the dissipation of the Δ-P3 scheme for $\nu=1/2$ and its dispersion,

for v far from this value. The accurate eigenvalue is identified by the "condition of consistency", with the exact amplification factor, $e^{-j\nu\beta}$:

$$\lambda_1(\beta, v) \underset{\beta\to 0}{\to} 1 \quad \forall v \in [0,1]. \tag{11}$$

We then identify the accurate eigenvalue:

$$\lambda_1(\beta, v) = (v-1)(v^2+v-1) + ve^{-j\beta}(3v - v^2 - 1) + v\sqrt{D}.$$

The remaining eigenvalue, $\lambda_2(\beta, v)$, is clearly inconsistent with (1), since

$$\lambda_2(\beta, v) \underset{\beta\to 0}{\to} 6v(v-1).$$

By using the equivalency (8), we then obtain the result

$$\tau(x,t) = -\frac{v}{72}(v-1)(1-v+v^2)\frac{\Delta x^4}{\Delta t} \times u_{4x} + \text{following terms.} \tag{12}$$

This result shows that the Δ-P3 scheme discretizes (1) with a third-order accuracy. Moreover, the modified equation of (1) by this scheme can be specified:

$$u_t + au_x = \frac{v}{72}(v-1)(1-v+v^2)\frac{\Delta x^4}{\Delta t} \times u_{4x}. \tag{13}$$

The stability condition prescribes that the coefficient in front of the fourth derivative of u, be negative. Since v is positive and there are no real roots for the polynomial $(1 - v + v^2)$, the only solution is therefore: $v \leqslant 1$, which is the typical CFL condition for an explicit scheme that discretizes (1). However, this analysis only predicts the behaviour of the low-frequency waves ($\beta \to 0$). To gain more insight on the behaviour for high frequencies, let us plot $|\lambda_{1,2}(\beta, v)| = f(\beta)$ or $f(N)$, for v fixed.

In such a case, N is defined as the number of cells-per-wavelength ($N \times \beta = 2\pi$) required to maintain dissipation and dispersion within acceptable bounds. This parameter is a very relevant characteristic in the acoustic context. For example, if we consider a computation in which the wave of a given wavelength has to be propagated over a range of R wavelengths, then the number of time steps required to propagate this wave, is $R \times N/v$. Therefore, the total amplitude error when a wave has moved R number of wavelengths can be expressed as

$$(1 - |\lambda_1(\beta, v)|^{R\times N/v}) \quad \text{with } |\lambda_1(\beta, v)| \leqslant 1 \qquad \forall \beta \in [0, \pi], \forall v \leqslant 1.$$

Similarly, the overall phase error can be calculated:

$$R \times \left(\frac{\mathrm{Arg}(\lambda_1(\beta, v))}{v\beta} - 1\right).$$

If $R = 100$, which is a typical value in many acoustic configurations, $N = 15$ cells-per-wavelength and the amplitude error per time step $D = 0.01\%$ for a given scheme, the total amplitude error reaches then 25%; for $N = 10$, this error decreases to 18% and for $N = 8$, we get an error of 15%. In what follows, as targets for accuracy, we will assume that the position of a wave (quantified by the phase error per time step, $E(\beta, v)$) and its amplitude (amplitude error per time step, $D(\beta, v)$), is required to within 0.01% for N roughly around the value 10.

Fig. 2 plot the amplitude of the accurate and spurious eigenvalues, for $v = 1/2$. At the highest frequency resolvable by the mesh, $\beta = \pi$ (two cells-per-wavelength), the accurate component of the numerical solution is attenuated with a minimum value for $|\lambda_1|$ ($|\lambda_1| = 0.866$); this is mainly due to the fact that the first term in the truncation error consists of the diffusive gradient, u_{4x}. Similarly, the damping of the spurious component by the eigenvalue λ_2, obviously appears. More precisely, let us consider Fig. 3, which show amplitude

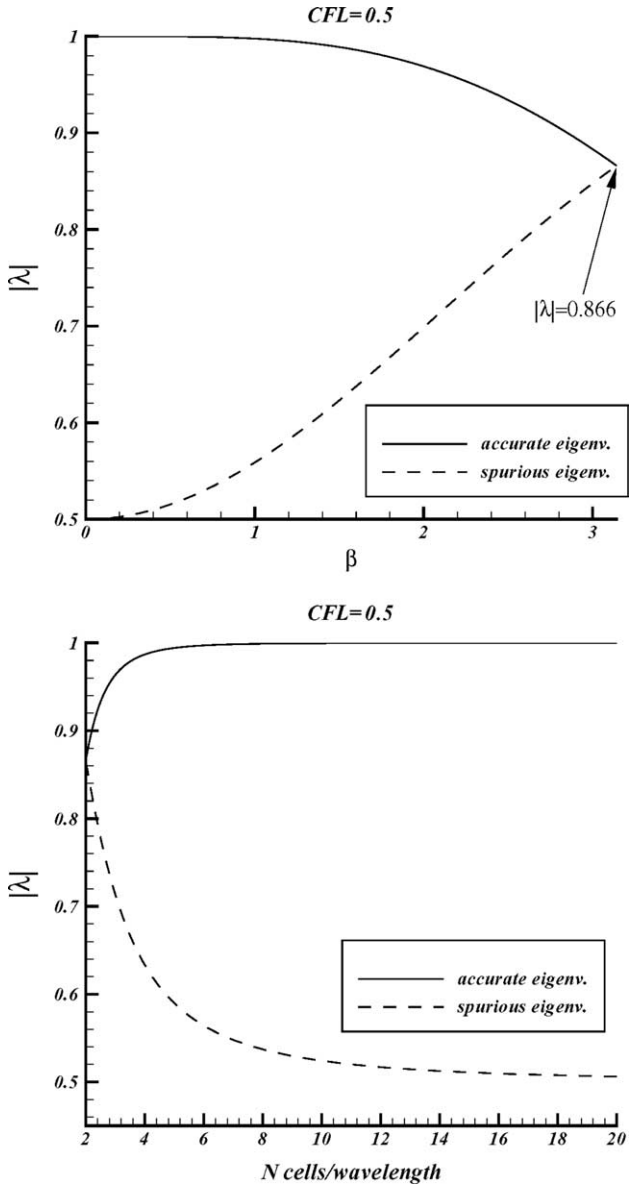

Fig. 2. Δ-P3 scheme: accurate and spurious eigenvalues amplitudes ($v = 0.5$) for the discretization of $u_t + au_x = 0$.

and phase error trends for the Δ-P3 scheme. The contours are plotted for several levels of dissipation and dispersion errors, in a plane that shows the number of cells-per-wavelength, N, versus Courant number, v.

It is important to notice some characteristics. Initially, as we can note it, the symmetry relations, (10), are verified for the dissipation (maximum of the error for $v = 1/2$) and the dispersion (zero error for $v = 1/2$). Then, for the range of valid Courant numbers ($0 \leqslant v \leqslant 1$), the Δ-P3 scheme presents an error of phase much less important than the error of dissipation. One good feature is that the scheme tends to be more accurate in the Courant number range $1/2 \leqslant v \leqslant 1$, since it needs less cells-per-wavelength to reach a given level of

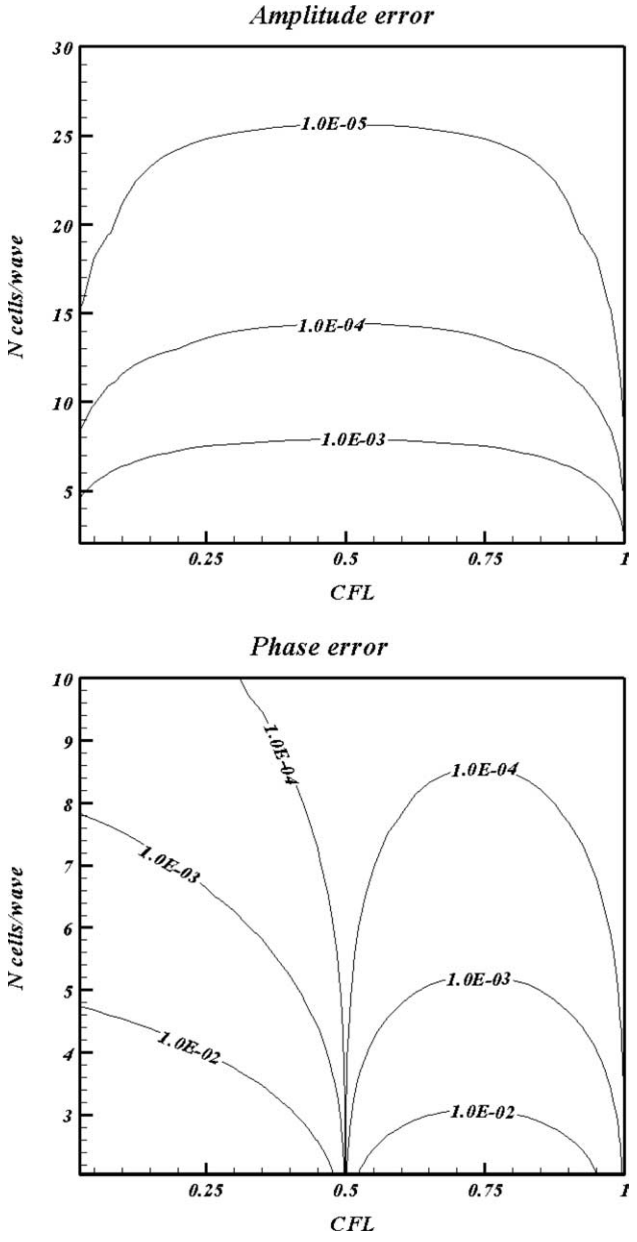

Fig. 3. Δ-P3 scheme: amplitude and phase errors trends for the scalar advection equation $u_t + au_x = 0$.

error, than for $0 \leqslant \nu \leqslant 1/2$. In the range $1/2 \leqslant \nu \leqslant 1$, one needs less than 15 cells-per-wavelength to reach the limit of 0.01%. Lastly, Fig. 4 plots the phase error in L_1-norm versus the phase angle, in logarithmic scales, for $\nu = 1/4$. Except for the highest frequencies, the slope of the curve (order of accuracy plus 1) indicates a spatial order of accuracy of 3 for the Δ-P3 scheme.

In order to compare with an optimized scheme for wave propagation problems, we use the well-known fourth-order (seven-point stencil) DRP scheme of Tam and Webb [11]. The temporal integration

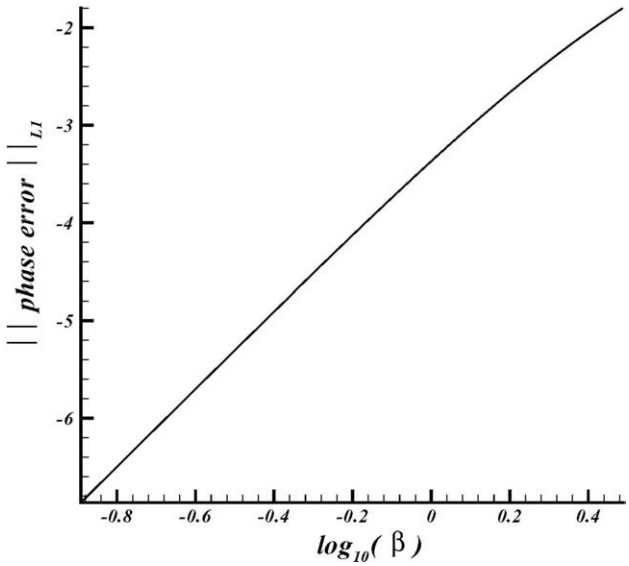

Fig. 4. Δ-P3 scheme: phase error for the scalar advection equation $u_t + au_x = 0$ ($v = 0.25$).

is performed by using the low dissipation and dispersion Runge–Kutta (LDDRK) scheme of Hu et al. [12]; this LDDRK time stepping method uses six stages and is fourth-order accurate, with a low storage recursive implementation. The result is a scheme which is fourth-order accurate in both time (LDDRK) and space (DRP): this scheme will be referred thereafter as the ''LDDRK6–DRP scheme''.

Fig. 5 produces dispersion and dissipation errors for such a scheme. As indicates it its symmetric stencil in space, this scheme produces an amplitude error on a very low level. However, by comparing with the Δ-P3 scheme, we can note that the LDDRK6–DRP scheme produces a considerable dispersion error: 19 cells-per-wavelength become necessary to reach the target accuracy of 0.01% in the phase error, whereas the Δ-P3 scheme only needs 9 cells-per-wavelength in the range $\frac{1}{2} < v < 1$. Therefore, these results demonstrate that, with roughly 15 cells-per-wavelength, the Δ-P3 scheme makes it possible to reach an accuracy of 0.01% of error in phase and in amplitude.

2.3. Accuracy comparisons

We test the accuracy of our scheme on the model-problem: $u_t + u_x = 0\ \forall x \in [0, 1]$. With the initial condition, $u(x, t = 0) = \sin(2\pi x)$ and 2-periodic boundary conditions, we compute the solution up to $t = 10$, i.e. after 10 time-periods. A uniform mesh with N cells is used for all the test cases. The CFL number is taken to 0.75 for both Δ-P3 and LDDRK6–DRP schemes. The results are shown in Tables 1 (Δ-P3) and 2 (LDDRK6–DRP). First, we can see that both schemes, achieve their designed order of accuracy. However, the Δ-P3 scheme produces better levels of error on coarse meshes: consequently, with only a third-order accuracy, the Δ-P3 scheme produces an error level similar with an optimized fourth-order scheme. Finally, Fig. 6 compares both schemes in terms of CPU efficiency: in such a case, the best performance is observed with the Δ-P3 scheme.

Therefore, based on this comparison, we can conclude that the gain in resolution obtained by using a compact hermitian and upwind third-order scheme, outweighs the associated greater algebraical com-

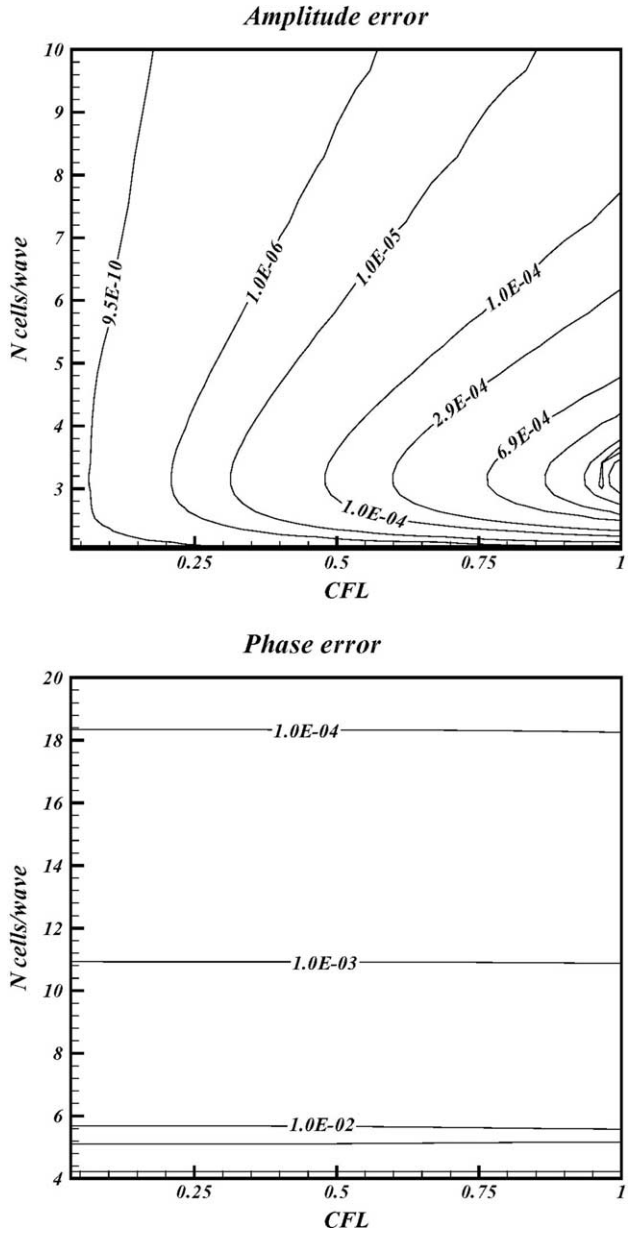

Fig. 5. LDDRK6–DRP scheme: amplitude and phase errors trends for the scalar advection equation $u_t + au_x = 0$.

plexity. In the 1-D context, compared with a more conventional fourth-order scheme, even optimized, the Δ-P3 scheme offers better performances in terms of resolution versus computational cost. In the section which follows, we generalize the Δ-P3 scheme to bi-dimensional problems in order to model linear acoustics.

Table 1
$u_t + u_x = 0$; $u(x,t = 0) = \sin(2\pi \times x)$; Δ-P3 scheme with periodic boundary conditions; $t = 10$; $v = 0.75$; L_1 and L_∞ errors

N	L_∞ error	L_∞ order	L_1 error	L_1 order
10	5.64×10^{-2}	–	3.61×10^{-2}	–
20	6.33×10^{-3}	2.90	4.03×10^{-3}	2.90
40	7.39×10^{-4}	2.97	4.71×10^{-4}	2.97
80	8.91×10^{-5}	3	5.67×10^{-5}	3
160	1.09×10^{-5}	3	6.96×10^{-6}	3
320	1.35×10^{-6}	3	8.62×10^{-7}	3

Table 2
$u_t + u_x = 0$; $u(x, t = 0) = \sin(2\pi \times x)$; LDDRK6–DRP scheme with periodic boundary conditions; $t = 10$; $v = 0.75$; L_1 and L_∞ errors

N	L_∞ error	L_∞ order	L_1 error	L_1 order
10	0.20	–	0.13	–
20	1.36×10^{-2}	3.60	8.65×10^{-3}	3.60
40	8.12×10^{-4}	3.70	5.17×10^{-4}	3.70
80	4.89×10^{-5}	4	3.11×10^{-5}	4
160	3.0×10^{-6}	4	1.90×10^{-6}	4
320	1.85×10^{-7}	4	1.18×10^{-7}	4

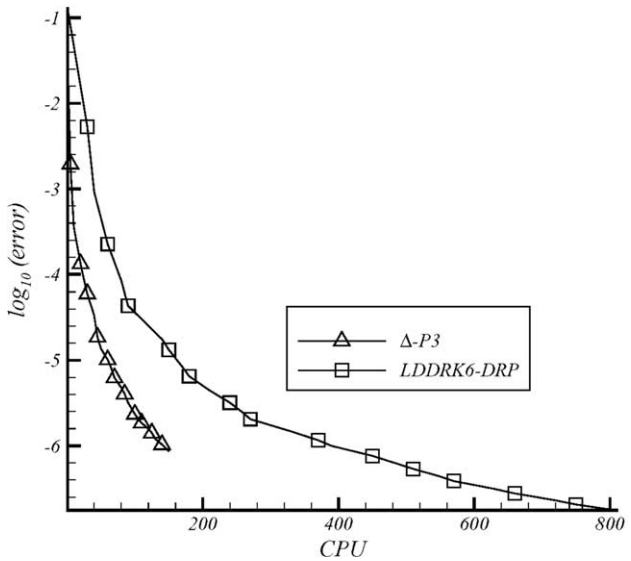

Fig. 6. Linear advection $u_t + u_x = 0$ ($u(x, t = 0) = \sin(2\pi \times x)$ $\forall x \in [0,1]$). L_1-error by CPU time for Δ-P3 and LDDRK6–DRP schemes. $t = 10$, $v = 0.75$, $N = 20 \rightarrow 320$ points.

3. High order upwind schemes for the acoustic equations

3.1. The governing equations

The wave propagation in a stationary and uniform mean flow can be modelled by a first-order system of equations with constant coefficients: the acoustic equations. In two dimensions, this leads to a system of three equations for three fluctuation variables, the pressure, p, and the two components of velocity, u and v.

In Cartesian coordinates (x,y,t), the acoustic equations in dimensionless form can be written as follows:

$$\begin{cases} \frac{\partial p}{\partial t} + \left(\frac{\partial u}{\partial x} + \frac{\partial v}{\partial y} \right) = 0, \\ \frac{\partial u}{\partial t} + \frac{\partial p}{\partial x} = 0, \\ \frac{\partial v}{\partial t} + \frac{\partial p}{\partial y} = 0. \end{cases} \tag{14}$$

It is a hyperbolic set of linear partial differential equations. Its solution can be broken up into "simple waves", [3]. In order to develop a compact upwind scheme that discretizes (14) while following the work initiated in the previous section, we wish to decompose the time-derivatives in a truly multi-dimensional way: it is the "decomposition stage".

3.2. Decomposition of the time-derivatives: the "decomposition stage"

To simplify what follows, we introduce a set of generic variables U, V, P. Hence, in order to discretize (14) with a third-order accuracy, we need to define

$$P \equiv \begin{cases} p \\ r_p \equiv p_x \\ s_p \equiv p_y \\ p_{xx}, p_{xy}, p_{yy} \\ p_{3x}, p_{xxy}, p_{xyy}, p_{3y} \end{cases}, \quad U \equiv \begin{cases} u \\ r_u \equiv u_x \\ s_u \equiv u_y \\ u_{xx}, u_{xy}, u_{yy} \\ u_{3x}, u_{xxy}, u_{xyy}, u_{3y} \end{cases}, \quad V \equiv \begin{cases} v \\ r_v \equiv v_x \\ s_v \equiv v_y \\ v_{xx}, v_{xy}, v_{yy} \\ v_{3x}, v_{xxy}, v_{xyy}, v_{3y} \end{cases}. \tag{15}$$

In order to calculate the temporal terms of order two and three which are necessary in the developments in Taylor series, we need to know the temporal evolution of the space-derivative of order 2 and 3 of the variables (u, v, p).

Thus, while using the linearity of (14), the generic variables, U, V, P, are solution of

$$\begin{cases} \frac{\partial P}{\partial t} + \left(\frac{\partial U}{\partial x} + \frac{\partial V}{\partial y} \right) = 0, \\ \frac{\partial U}{\partial t} + \frac{\partial P}{\partial x} = 0, \\ \frac{\partial V}{\partial t} + \frac{\partial P}{\partial y} = 0. \end{cases} \tag{16}$$

This form is merely the initial form (14) with an enlargement of the variables.

According to the general principles stated in [4], we have developed a specific "four-wave model" which preserves the linearity of (16). The time-derivatives are decomposed into four simple waves, according to the formula:

$$\begin{bmatrix} P_t \\ U_t \\ V_t \end{bmatrix} = -\frac{1}{2} \left(\psi_1 \begin{bmatrix} 1 \\ -n_y \\ n_x \end{bmatrix} + \psi_2 \begin{bmatrix} 1 \\ n_x \\ n_y \end{bmatrix} + \psi_3 \begin{bmatrix} 1 \\ n_y \\ -n_x \end{bmatrix} + \psi_4 \begin{bmatrix} 1 \\ -n_x \\ -n_y \end{bmatrix} \right). \tag{17}$$

$\vec{n} \equiv (n_x, n_y)^t \equiv (\cos\theta, \sin\theta)^t$ is a unit vector in the direction of wave propagation and ψ_p is defined as the wave-strength (or amplitude) of the pth wave. We can rewrite this relation in an equivalent way as

$$\Delta t \times \begin{bmatrix} P_t \\ U_t \\ V_t \end{bmatrix} = \Delta\Phi_1 + \Delta\Phi_2 + \Delta\Phi_3 + \Delta\Phi_4. \tag{18}$$

$\Delta\Phi_p \equiv -\frac{\Delta t}{2}\psi_p \begin{bmatrix} 1 \\ \vec{n}_p \end{bmatrix}$ is then defined as the perturbation (or "fluctuation") in the variables (U, V, P) caused by the pth wave which propagates in the direction given by $\vec{n}_p$.

As the name indicates it, four simple acoustic waves are employed to model the acoustic regime at any discrete point. These four waves are propagated in orthogonal directions the ones with the others. One of these four waves has an angle of orientation located in the interval [0, π/2] and we take it as reference; its orientation is given by the angle, θ, and its amplitude is ψ_2. The strength of the wave that moves in the opposite direction will be ψ_4 and the waves that travel at right angles to these two, have strengths ψ_1, ψ_3, Fig. 7. The first important characteristic that determines our model is the orientation angle, θ, arbitrarily imposed to the value π/4.

Such a model is built on the basis of physical arguments and to facilitate obtaining the algebraic solution. Firstly, with an orientation angle imposed, the acoustic waves only represent four degrees of freedom: the four wave strengths ψ_p now become solution of a linear set of equations. Secondly, this set of four orthogonal acoustic waves permits to model the isotropic nature of an acoustic problem: the effect of acoustic waves with the same strength integrated over all possible directions, can be represented by four mutually perpendicular waves [4].

However it is worth to notice that any arrangement of three waves whose directions are separated from an angle of 2π/3, would produce, locally, the same effect. Finally, the choice $\theta = \pi/4$, is the best in order to avoid algorithmic difficulties due to possible alignment of the propagation directions with the grid directions.

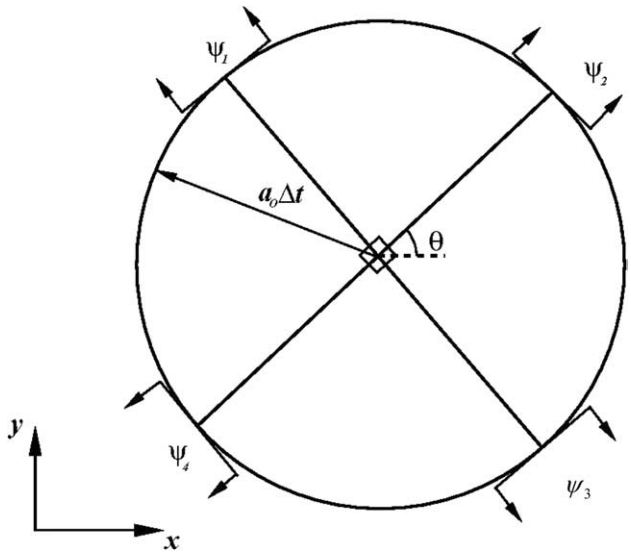

Fig. 7. Δ-P3 scheme: acoustic waves comprising the discrete model for linear acoustics.

Although drawn aside by Roe for the discretization of the equations of Euler [4], this choice is not also problematic when one wishes to discretize acoustic problems. Indeed, only the acoustic waves intervening in the unsteady part of the equations must be considered. Therefore, the possible existence of non-realistic waves created by an arbitrary decomposition, is left out. Then, in theory, the only drawback of an arbitrary specified orientation angle, θ, is an increasing of the dissipative nature of the scheme when θ does not coincide with the main physical meaningful direction. However, the choice of a ''four-wave pattern'' is designed to minimize this drawback.

To close the model, we must solve for the amplitudes ψ_1, ψ_2, ψ_3, ψ_4. By combining (16) and (17), these four unknowns become solution of the following linear system:

$$\begin{cases} \frac{1}{2}(\psi_1+\psi_2+\psi_3+\psi_4) = U_x + V_y, \\ \frac{1}{2}[(\psi_3-\psi_1)n_y + (\psi_2-\psi_4)n_x] = P_x, \\ \frac{1}{2}[(\psi_1-\psi_3)n_x + (\psi_2-\psi_4)n_y] = P_y. \end{cases} \tag{19}$$

It is an undetermined linear system since there are four unknowns for only three equations. After successive trials and errors, we propose the following solution:

$$\begin{cases} \psi_1 \equiv -P_\tau + \frac{1}{2}(U_x+V_y), \quad \psi_4 \equiv -P_n + \frac{1}{2}(U_x+V_y), \\ \psi_2 \equiv P_n + \frac{1}{2}(U_x+V_y), \quad \psi_5 \equiv P_\tau + \frac{1}{2}(U_x+V_y) \end{cases} \tag{20}$$

with

$$\begin{cases} P_n \equiv n_x P_x + n_y P_y, \\ P_\tau \equiv n_y P_x - n_x P_y. \end{cases}$$

If we consider the arbitrariness of the decomposition (17), the non-uniqueness of (20) is not so decisive, even if solutions that are more accurate can exist. In connection with the choice $\theta \equiv \pi/4$, formulae (20) allow us to close this four-wave decomposition of the time-derivatives.

Some interesting properties of this model must be emphasized.

- It is a multi-dimensional decomposition, since the acoustic waves are entirely independent upon the underlying grid, whatever the mesh, structured or unstructured (Fig. 8). The only important matter is to determine the simple wave which moves towards a discrete point and contributes to update the unknowns at this point.
- The same acoustic simple wave brings fluctuations (or perturbations) that update the solution and all its derivatives: the advantage of linearity is then maintained.
- Since decomposition (17) accounts for the isotropic nature of the acoustic waves, the particular value of the propagation angle, θ, has no real physical importance as long as it is kept free of the numerical data.
- At any discrete point, i, the decomposition (17) combined with (20), yields, for instance, the following result for the generic variable P (see Fig. 8):

$$\begin{aligned} P_t|_i = -\frac{1}{2}\sum_{j=1}^{4}\psi_j \equiv -\frac{1}{2}\Bigg\{ &\left[-P_\tau + \frac{1}{2}(U_x+V_y)\right]_1 + \left[P_n + \frac{1}{2}(U_x+V_y)\right]_2 \\ &+ \left[P_\tau + \frac{1}{2}(U_x+V_y)\right]_3 + \left[-P_n + \frac{1}{2}(U_x+V_y)\right]_4 \Bigg\}. \end{aligned} \tag{21}$$

At the differential level, this sum can be simplified, since

$$-P_\tau|_1 + P_n|_2 + P_\tau|_3 - P_n|_4 \equiv 0$$

at the same discrete point, i.

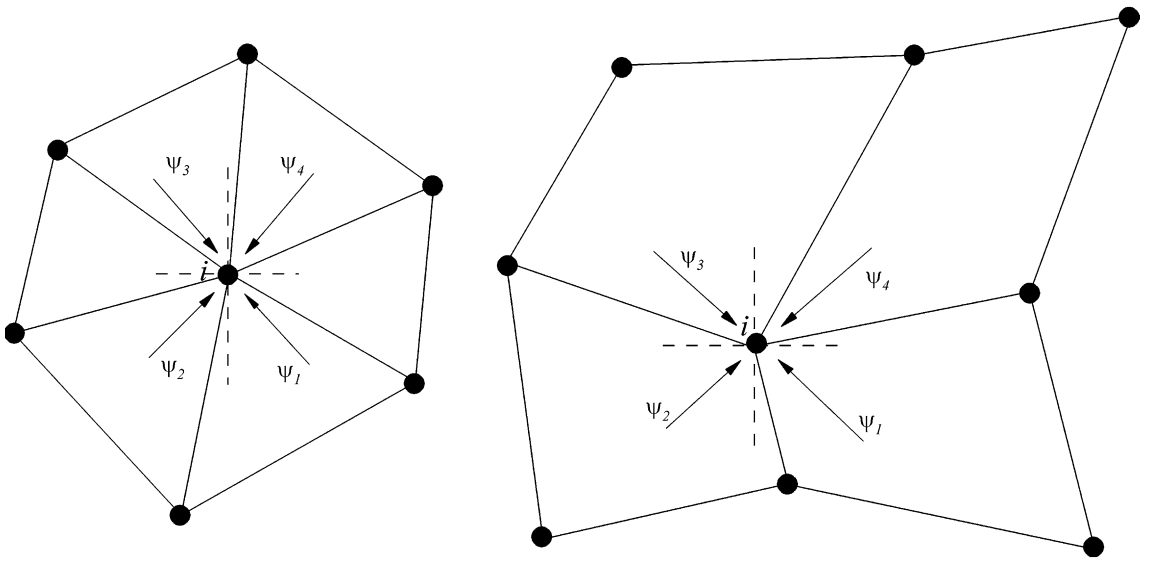

Fig. 8. Δ-P3 scheme: multi-dimensional wave decomposition for linear acoustics – unstructured mesh (left), structured mesh (right).

However, to discretize $P_t|_i$ with the formula:

$$P_t|_i = -\frac{1}{4}\{(U_x + V_y)_1 + (U_x + V_y)_2 + (U_x + V_y)_3 + (U_x + V_y)_4\}$$

would be awkward since it would produce an unstable centred discretization for the generic variable, P.

Indeed, at the discrete level, the term $-P_\tau|_1 + P_n|_2 + P_\tau|_3 - P_n|_4$ is crucial and represents the total truncation error generated by the discretization. As demonstrated in the previous section, this truncation error is dissipative. By adding a dissipative term, this truncation error stabilizes the numerical scheme and makes it upwind.

Now, we determine the form of the local spatial interpolator that characterizes the overall accuracy of the resulting scheme, namely the "reconstruction stage".

3.3. The form of the local spatial interpolator: the reconstruction stage

In this section, we consider a Cartesian grid with uniform spacing, h, in both space directions. The discrete unknowns (the function and its first derivatives) are stored at the vertices of the mesh. We define a generic cell of which the vertices are numbered according to the decomposition (17). Thus, the point 2 is updated, in the cell considered, by the local wave, ψ_2, which moves in its direction, Fig. 9.

It is important to notice that there are no weighting factors distributing the effects of each wave over the vertices. In other words, the point 2 is only affected by the wave ψ_2 in the cell depicted by Fig. 9: it is the advantage of using simple waves of which the orientation is assumed in advance.

To simplify, let us introduce the generic variable:

$$\varphi \equiv \begin{cases} p \\ u\,. \\ v \end{cases} \tag{22}$$

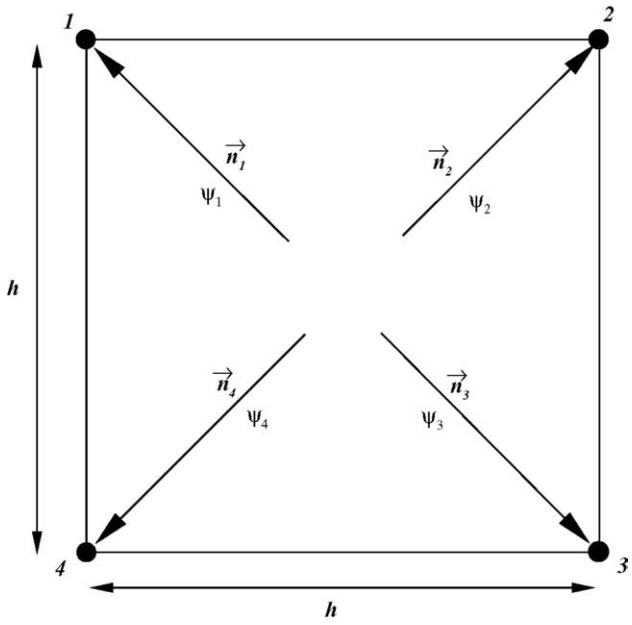

Fig. 9. Generic cell: numbering of the vertices according to the multi-dimensional wave decomposition for linear acoustics.

We then define, on the generic cell (1, 2, 3, 4), the local interpolator of φ, namely $\tilde{\varphi}(x, y)$, at the discrete time $t_n \equiv n\Delta t$. There are 10 degrees of freedom in a cubic representation of $\tilde{\varphi}(x, y)$, so working with cubic elements requires storing, at least, 10 quantities for each discrete cell. So, if we consider the following form:

$$\tilde{\varphi}(x, y) \equiv c_1 + c_2 x + c_3 y + c_4 xy + c_5 x^2 + c_6 y^2 + c_7 x^2 y + c_8 xy^2 + c_9 x^3 + c_{10} y^3 \tag{23}$$

which only necessitates 10 pieces of data to be uniquely determined, a difficulty arises with the adapted choice of these data. For example, if we discard two pieces of data, say: r_φ, s_φ, from the point 4, we can then completely define (23) by using the 10 remaining variables at the vertices (1, 2, 3, 4).

However, by doing so, we introduce an artificial distinction between the point 4 and the others, without any physical justification: this discrepant treatment may create numerical instabilities or inaccuracies when the fluctuations are assembled.

In order to prevent this problem, we need to define and calculate (23), for each point that defines the cell (1, 2, 3, 4). For example, in order to calculate the fluctuation caused by the wave ψ_2, $(\Delta\Phi_2)$, which moves towards the point 2, we calculate (23) by discarding the data r_φ and s_φ at the point 4 (see Fig. 10). In an opposite way, the fluctuation generated by the wave ψ_4, $(\Delta\Phi_4)$, which updates the point 4, will be calculated by using (23), now defined by eliminating the data (r_φ, s_φ) at the point 2. The same principle is worth for the points 1 and 3.

In this way, each point constituting the cell (1, 2, 3, 4) will undergo the same treatment. Consequently, this solution will necessitate the calculation of four polynomials (23) in each cell. In other words, each wave will be calculated by its own polynomial. As in the previous section, the expansion coefficients $\{c_i\}$, are obtained from the known data at the vertices of the mesh, by the following relationships:

$$\begin{cases} \tilde{\varphi}(x_i, y_i) = \varphi_i, \\ \tilde{\varphi}_x(x_i, y_i) = r_\varphi|_i, \\ \tilde{\varphi}_y(x_i, y_i) = s_\varphi|_i. \end{cases}$$

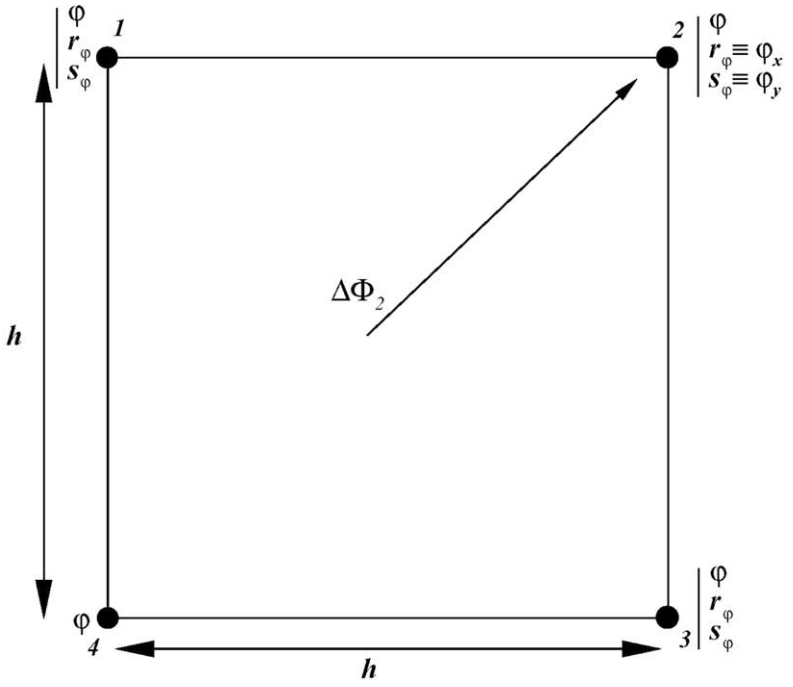

Fig. 10. Δ-P3 scheme: definition of the discrete stencil for the local interpolator at the point 2 on the generic cell (1, 2, 3, 4): $\tilde{\varphi}(x,y) \equiv c_1 + c_2x + c_3y + c_4xy + c_5x^2 + c_6y^2 + c_7x^2y + c_8xy^2 + c_9x^3 + c_{10}y^3$.

These relations generate a linear system of 10 equations for the 10 unknowns $\{c_i\}$. This system can be formally inverted by using the MAPLE symbolic mathematical computer package. By doing so, we are able to calculate all the derivatives which we need in the calculation of the wave strengths, ψ_p. For instance, the second derivatives of the generic variable φ, calculated at the point 2, are the following:

$$\begin{cases} h^2 \times \tilde{\varphi}_{xx}\big|_2 = 2 \times \left[h \times (r_\varphi|_1 + 2r_\varphi|_2) + 3(\varphi_1 - \varphi_2)\right], \\ h^2 \times \tilde{\varphi}_{xy}\big|_2 = \left[h \times (r_\varphi|_2 - r_\varphi|_3 + s_\varphi|_2 - s_\varphi|_1) + \varphi_1 - \varphi_2 + \varphi_3 - \varphi_4\right], \\ h^2 \times \tilde{\varphi}_{yy}\big|_2 = 2 \times [h \times (s_\varphi|_3 + 2s_\varphi|_2) + 3(\varphi_3 - \varphi_2)], \end{cases} \tag{24}$$

and the third derivatives are

$$\begin{cases} h^3 \times \tilde{\varphi}_{3x}\big|_2 = 6 \times [2(\varphi_1 - \varphi_2) + h \times (r_\varphi|_2 + r_\varphi|_1)], \\ h^3 \times \tilde{\varphi}_{xxy}\big|_2 = 2 \times [\varphi_1 - \varphi_2 + \varphi_3 - \varphi_4 + h \times (r_\varphi|_2 - r_\varphi|_3)], \\ h^3 \times \tilde{\varphi}_{xyy}\big|_2 = 2 \times [\varphi_1 - \varphi_2 + \varphi_3 - \varphi_4 + h \times (s_\varphi|_2 - s_\varphi|_1)], \\ h^3 \times \tilde{\varphi}_{3y}\big|_2 = 6 \times [2(\varphi_3 - \varphi_2) + h \times (s_\varphi|_2 + s_\varphi|_3)]. \end{cases} \tag{25}$$

Now, we need to detail the procedure developed in order to update the variables and its derivatives: the "evolution stage".

3.4. The evolution stage

We strictly follow the "Cauchy–Kovaleskaya procedure" detailed in the previous section in order to update the discrete solution and its derivatives in an upwind way.

After having calculated $\tilde{\varphi}(x,y)$, for each point defining the discrete stencil:

(a) We expand in Taylor series in time, up to the order 3, $\varphi(x_i, y_i, t_n + \Delta t)$ around the basis point (x_i, y_i, t_n):

$$\varphi_i^{n+1} = \varphi_i^n + \Delta t \times \varphi_t|_i^n + \frac{\Delta t^2}{2}\varphi_{tt}|_i^n + \frac{\Delta t^3}{6}\varphi_{3t}|_i^n + \mathrm{O}(\Delta t^4).$$

(b) We expand in Taylor series in time, up to the order 2, the derivatives of φ, (r_φ, s_φ):

$$r_\varphi|_i^{n+1} = r_\varphi|_i^n + \Delta t \times (r_\varphi)_t|_i^n + \frac{\Delta t^2}{2}(r_\varphi)_{tt}|_i^n + \mathrm{O}(\Delta t^3).$$

(c) We substitute the temporal derivatives by their spatial counterparts, by applying a Cauchy–Kovaleskaya procedure. For instance, the pressure variable, p, is written:

$$p_i^{n+1} = p_i^n + \Delta t \times \underbrace{p_t|_i^n}_{-(u_x+v_y)|_i^n} + \frac{\Delta t^2}{2}\underbrace{p_{tt}|_i^n}_{-(u_{xt}+v_{yt})|_i^n} + \frac{\Delta t^3}{6}\underbrace{p_{3t}|_i^n}_{(p_{xxt}+p_{yyt})|_i^n} + \mathrm{O}(\Delta t^4)$$

and its derivative, $r_p \equiv p_x$, in the x-direction:

$$r_p|_i^{n+1} = r_p|_i^n + \Delta t \times \underbrace{(r_p)_t|_i^n}_{-(u_{xx}+v_{xy})|_i^n} + \frac{\Delta t^2}{2}\underbrace{(r_p)_{tt}|_i^n}_{-(u_{xxt}+v_{xyt})|_i^n} + \mathrm{O}(\Delta t^3).$$

(d) We truncate the previous series and we approximate the spatial derivatives by using the local interpolator, $\tilde{\varphi}(x,y)$. Hence, we get the following set of equations for $(\varphi, r_\varphi, s_\varphi)$ that discretizes (16) at the discrete point i:

$$\begin{cases} p_i^{n+1} = p_i^n - \Delta t \times (r_u + s_v)|_i^n - \frac{\Delta t^2}{2}[(r_u)_t + (s_v)_t]|_i^n + \frac{\Delta t^3}{6}[(\tilde{p}_{xx})_t + (\tilde{p}_{yy})_t]|_i^n, \\ u_i^{n+1} = u_i^n - \Delta t \times r_p|_i^n - \frac{\Delta t^2}{2}[(r_p)_t]|_i^n + \frac{\Delta t^3}{6}[(\tilde{u}_{xx})_t + (\tilde{v}_{xy})_t]|_i^n, \\ v_i^{n+1} = v_i^n - \Delta t \times s_p|_i^n - \frac{\Delta t^2}{2}[(s_p)_t]|_i^n + \frac{\Delta t^3}{6}[(\tilde{u}_{xy})_t + (\tilde{v}_{yy})_t]|_i^n, \end{cases} \tag{26}$$

$$\begin{cases} r_p|_i^{n+1} = r_p|_i^n + \Delta t \times (r_p)_t|_i^n - \frac{\Delta t^2}{2}[(\tilde{u}_{xx})_t + (\tilde{v}_{xy})_t]|_i^n, \\ r_u|_i^{n+1} = r_u|_i^n + \Delta t \times (r_u)_t|_i^n - \frac{\Delta t^2}{2}(\tilde{p}_{xx})_t|_i^n, \\ r_v|_i^{n+1} = r_v|_i^n + \Delta t \times (r_v)_t|_i^n - \frac{\Delta t^2}{2}(\tilde{p}_{xy})_t|_i^n. \end{cases} \tag{27}$$

For the derivatives in the y-direction, we obtain the following results:

$$\begin{cases} s_p|_i^{n+1} = s_p|_i^n + \Delta t \times (s_p)_t|_i^n - \frac{\Delta t^2}{2}[(\tilde{u}_{xy})_t + (\tilde{v}_{yy})_t]|_i^n, \\ s_u|_i^{n+1} = s_u|_i^n + \Delta t \times (s_u)_t|_i^n - \frac{\Delta t^2}{2}(\tilde{p}_{xy})_t|_i^n, \\ s_v|_i^{n+1} = s_v|_i^n + \Delta t \times (s_v)_t|_i^n - \frac{\Delta t^2}{2}(\tilde{p}_{yy})_t|_i^n. \end{cases} \tag{28}$$

(e) All the time-derivatives arising in (26)–(28) are decomposed by using the definition (15) and the general form (17) with the result (20). More exactly, the time-derivatives are decomposed in four simple acoustic waves. This procedure results in a decomposition of (26)–(28) along each simple wave and permits to identify the temporal fluctuation brought by each wave. This step is crucial in the discretization process since it makes upwind the resulting scheme.
(f) According to the direction of each simple wave, the fluctuations are shared and gathered at any discrete point, in order to update the data, Fig. 11.

Thus, the reconstruction stage plus steps from (a) to (f) define the main characteristics of the "Δ-P3 scheme", for linear acoustics. To close the characterization of the Δ-P3 scheme, we need to specify the boundary procedure.

3.5. Boundary conditions for acoustics

Broadly speaking, the acoustic boundary conditions can be classified into two categories. They are

1. wall boundary conditions,
2. radiation boundary conditions.

In few words, the boundary conditions for linear acoustics consist in imposing that normal component of velocity is zero at the wall and the radiated sound waves leave the computation domain smoothly, without significant reflection. In this section, a set of radiation and wall boundary conditions compatible with the Δ-P3 scheme, is developed.

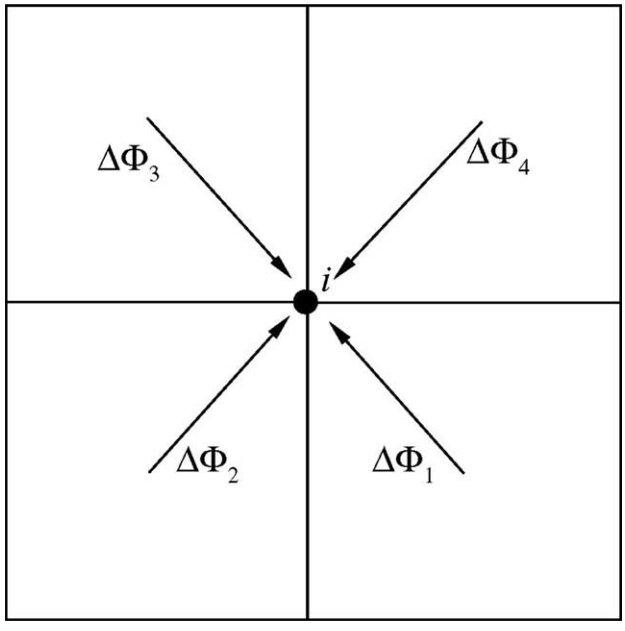

Fig. 11. Gathering of the temporal fluctuations along each simple wave for linear acoustics.

3.5.1. Wall boundary conditions

Let us suppose that the wall is flat and solid and lies along the y-axis. We consider the boundary conditions for any point, P, situated on this wall, Fig. 12.

The normal velocity u being zero at this point, whatever the time t, we then deduce the following conditions for the first derivatives of u, v, p, from (14):

$$u_P \equiv 0 \ \forall y, \forall t \ \Rightarrow \ \begin{cases} p_x|_P \equiv 0 & \forall y, \forall t, \\ u_y|_P \equiv 0 & \forall y, \forall t. \end{cases} \tag{29}$$

The remaining variables, which are not explicitly specified by (1), are updated by using the algebraical expressions defining the Δ-P3 scheme (formulae (26)–(28)). The contribution of the waves ψ_2 and ψ_3 is set to zero (Fig. 12) into these formulae since these waves do not physically exist. In other words, the remaining variables at the wall are only updated by the waves coming from the interior of the computational domain, ψ_1 and ψ_4.

In contrast with the centered schemes, such a procedure rules out the need for extra boundary conditions or "ghost points" behind the wall [5]. This can be considered as an advantage since the ghost point method generates the equivalent of non-zero waves ψ_2 and ψ_3, which correspond to spurious short wavelength numerical waves entering the calculation domain. In such a case, artificial selective damping terms must be added to provide numerical stability near the solid surface [7]. In this sense, our procedure can be qualified as a "non-reflecting wall boundary condition".

For example, if there is symmetry of the problem about the y-axis, the boundary procedure remains nearly identical, Fig. 13. Indeed, these conditions are

$$\left.\begin{matrix} u|_S \equiv 0 \\ v_x|_S \equiv 0 \end{matrix}\right\} \ \forall y, \forall t \ \Rightarrow \ \begin{cases} p_x|_S \equiv 0 & \forall y \\ u_y|_S = 0 \end{cases} \tag{30}$$

The procedure used to update the remaining variables is almost the same as the previous one except for the wave strengths ψ_2 and ψ_3 which are, respectively, set equal to ψ_1 and ψ_4, in order to simulate the symmetry condition for the acoustic waves, Fig. 13.

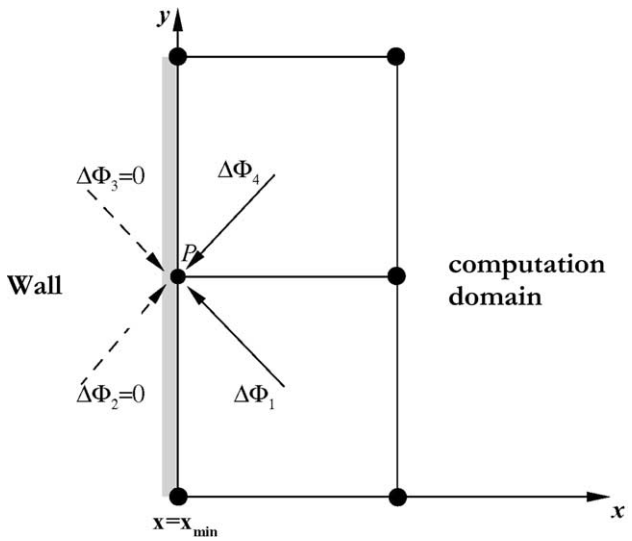

Fig. 12. Linear acoustics: wall boundary conditions for a solid wall located at $x = x_{\min}$.

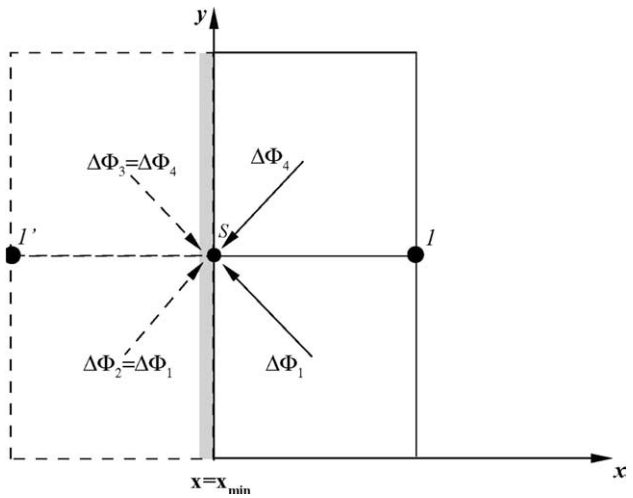

Fig. 13. Linear acoustics: symmetry boundary conditions about the y-axis.

3.5.2. Radiation boundary conditions

For exterior acoustic problems, a set of non-reflecting boundary conditions is necessary at the external boundaries. The purpose of these conditions is to permit the radiated sound waves to smoothly leave the computation domain, without non-physical reflection.

A great advantage of any wave decomposition of the time-derivatives is the possibility to discriminate the outgoing waves from the ingoing ones, at a given boundary.

Let us suppose that the line $y = y_{\max}$ is a radiation boundary, Fig. 14. Then, the points situated on this line will be actualized by using the two outgoing acoustic waves ψ_2 and ψ_1. The non-reflective boundary conditions will be ensured by setting the ingoing waves, ψ_4 and ψ_3, to zero, Fig. 14.

Such a procedure is designed to preserve the accuracy of the scheme at the boundary points while preventing the apparition of instabilities at these same points.

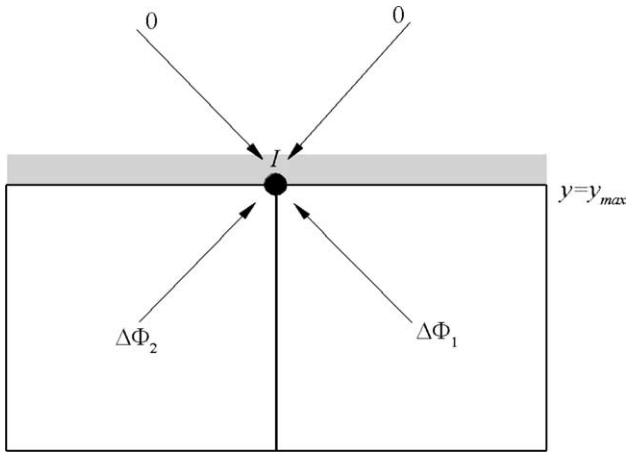

Fig. 14. Linear acoustics: radiation boundary conditions along the line $y = y_{\max}$.

4. Numerical tests

In this section, we present the results for numerical experiments made with the Δ-P3 scheme and we compare them with the fourth-order LDDRK6–DRP scheme.

Unless it is indicated, a square grid with uniform spacing, h, in the two space directions, is employed. The CFL number is thus defined by $\mathrm{CFL} \equiv \Delta t/h$. The decomposition of the time-derivatives is ensured by (17) and (20). The derivatives used to calculate the wave strengths are calculated according to Cartesian formulae (24) and (25), proposed in Section 3.3.

4.1. Accuracy comparisons

The numerical experiments are carried out with a doubly periodic solution of (14), for (x, y) defined in the domain $[-10, 10] \times [-10, 10]$. We use the following exact solution as reference:

$$\begin{cases} p(x,y,t) = \cos(2\pi\sqrt{2} \times t) \times \sin(2\pi \times x) \times \sin(2\pi \times y), \\ u(x,y,t) = -\frac{1}{\sqrt{2}} \sin(2\pi\sqrt{2} \times t) \times \cos(2\pi \times x) \times \sin(2\pi \times y), \\ v(x,y,t) = -\frac{1}{\sqrt{2}} \sin(2\pi\sqrt{2} \times t) \times \sin(2\pi \times x) \times \cos(2\pi \times y). \end{cases} \tag{31}$$

The numerical solution is computed until $t = 1$.

Grid refinement data are provided for mesh sizes going from 20×20 points to 300×300 points. The CFL number is taken equal to 0.45 for the Δ-P3 scheme and 0.10 for the LDDRK6–DRP scheme in order to obtain the best results in terms of resolution/computational cost. Fig. 15 plots the $\log_{10}$ of L_1-error in pressure against the $\log_{10}$ of the mesh size. As one can note it, both schemes exhibit the same behaviour though the Δ-P3 scheme slightly behaves better in terms of error level.

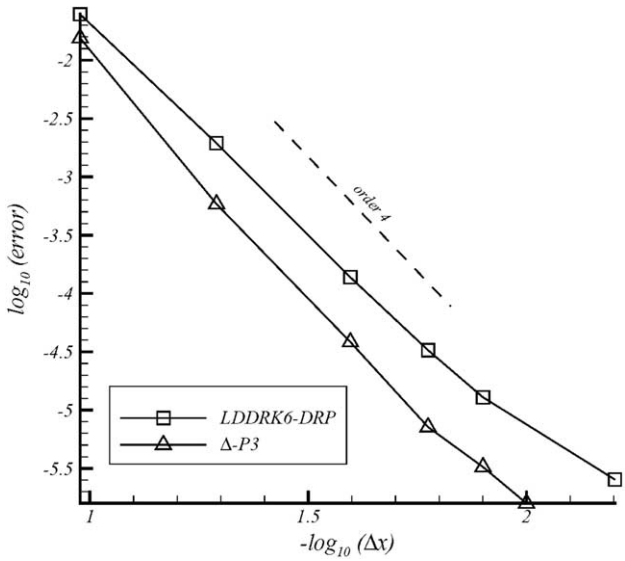

Fig. 15. Linear acoustics: doubly periodic solution, L_1-error by grid resolution, $t = 1$, Δ-P3 (CFL = 0.45) and LDDRK6–DRP schemes (CFL = 0.10).

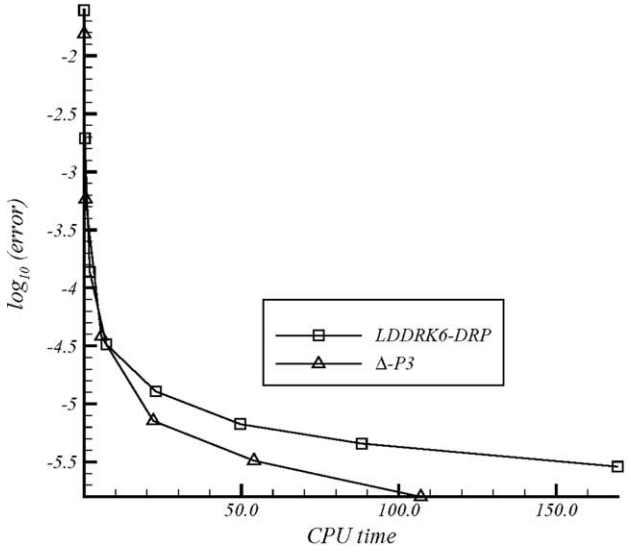

Fig. 16. Linear acoustics: doubly periodic solution, L_1-error by CPU time, $t = 1$, Δ-P3 (CFL = 0.45) and LDDRK6–DRP schemes (CFL = 0.10).

Fig. 16 presents the $\log_{10}$ of the L_1-error plotted against the CPU time required for each level of grid. The results obtained in Section 2 are confirmed: despite a greater algebraic complexity the Δ-P3 scheme is more effective. Thus, it demonstrates that the greatest algebraic complexity of the Δ-P3 scheme is not a disadvantage in terms of CPU cost when it is compared with a "state of the art" finite-difference method.

4.2. Acoustic pulse reflected from a rigid wall [9]

In order to show the effectiveness of the radiation and wall boundary conditions developed in this article, we consider, as a second example, an acoustic pulse reflected from a rigid wall. This problem indicated under the name of problem of "category IV" in [9] has an exact solution. An acoustic pulse is produced by an initial Gaussian distribution for the impulse of pressure. At the time $t = 0$, the initial conditions are as follows:

$$\begin{cases} u = v = 0, \\ p(x, y, 0) = \mathrm{e}^{-\left[10\times(x^2+(y+0.7)^2)\right]}. \end{cases}$$

The derivation of this condition makes it possible to initialize the derivative variables. The domain of solution is $-1 \leqslant x \leqslant 1$, $-1 \leqslant y \leqslant 1$, with the wall located at $y = -1$. Two boundary conditions are used: a wall condition along $y = -1$ and an acoustic radiation condition in the far field (top, left and right boundaries).

For the Δ-P3 scheme, radiation boundary conditions are imposed in the way detailed in Section 3.5.2, whereas wall boundary conditions at $y = -1$ follow the process defined in Section 3.5.1.

For the LDDRK6–DRP scheme, we use the boundary conditions proposed by Tam, [5]. In this way, the wall condition requires that the time rate of change of the normal velocity at the wall be zero: $\frac{\partial v}{\partial t} = 0 = \frac{\partial p}{\partial y}$.

The zero setting of the normal derivative of pressure at the wall while the other derivatives are computed in a traditional way, makes it possible to impose this condition. At the far field, the asymptotic radiation

boundary conditions detailed in [5], are imposed. For all the derivatives, one-sided five-point explicit stencils are used in order to preserve fourth-order accuracy at the boundaries. For both schemes, all computations are carried out on a 20×20 Cartesian mesh. A CFL number of 0.5 is employed in all simulations.

Fig. 17 gives the numerical results for the Δ-P3 scheme at $t = 1$, 1.2 and 1.4, when the impulse of pressure reflected from the wall and reached the far-field boundaries. Even on a so coarse mesh, the method functions correctly at the boundaries since no artificial reflections appear. Moreover, the comparisons between the solutions exact and calculated along a vertical cut at $x = 0$, show a good agreement. From the results given by Fig. 18, we can see that the DRP scheme suffers from a considerable error of dispersion on such a mesh: spurious short waves are generated at the boundaries and cannot be attenuated by the centred DRP scheme.

4.3. The two-dimensional piston problem [10]

The simulation of the acoustic field produced by an oscillating piston fixed on an infinite wall, Fig. 19, constitutes a good model problem to examine the capacity of a numerical scheme to treat the multi-dimensional wave propagation and its non-reflection at the boundaries. In dimensionless coordinates, the piston half-width is one unit and it oscillates at a rate such that the normal component of velocity to its surface is $u(t) = \cos(2\pi \times f \times t)$, with the frequency, f, selected as $f \in \{0.5, 1\}$. The computational domain is $0 \leqslant x \leqslant 20$ and $-10 \leqslant y \leqslant 10$. The exact solution to this problem is available in [10].

Firstly, let us consider the case $f = 0.5$. All computations are carried out on a 160×160 Cartesian mesh (16 cells-per-wavelength for the wave propagating along the symmetry line) and a CFL number of 0.5 is employed in all simulations. The derivative variables are initialized by zero. Time integration was carried out for 10 cycles of oscillation for the piston: this is a sufficient time so that the initial wave front created by the piston, reaches the opposite corner of the domain. Fig. 20 shows the results computed with the Δ-P3 scheme. With such a grid resolution, the results are good. As we can note it, there are no spurious waves at the boundaries: the outgoing acoustic waves leave smoothly the computation domain without any obvious spurious oscillation. This remains unchanged when the simulation time is increased. The non-reflective nature of the boundary conditions is clearly visible in Fig. 21.

Fig. 22 shows the solution computed with the LDDRK6–DRP scheme on the same grid: the dispersive nature of such a scheme is obvious when we consider the lateral pressure distribution at $x = 10$. To finish, Fig. 23 presents the numerical results for the solution that oscillates more, $f = 1$. With such a value, 320×320 grid points become necessary in order to get a good resolution with the Δ-P3 scheme (16 cells-per-wavelength for the wave propagating along the symmetry line). The agreement with the analytical results is very good. Fig. 24 shows contour plots of pressure profile calculated by the Δ-P3 scheme: the major part of acoustic energy is now transmitted along the x-axis and only one smaller part of this one is radiated diagonally. Once more, the non-reflective boundary conditions function correctly at the open boundaries, even when the time of simulation is increased.

4.4. Acoustic scattering from a cylinder [25]

This example is one of the second computational aero-acoustics benchmark problems [25]. The goal of this study is to check the effectiveness of curvilinear wall boundary and far field non-reflecting conditions, when a source term exists. For this problem, a 2-D cylinder of radius $R = 0.5$ is located at the origin. At time $t = 0$, a first impulse of pressure is initiated at the point S, Fig. 25. The solution of this problem is characterized by the temporal evolution of the pressure in three selected points: A ($r = 5$, $\theta = 90°$), B ($r = 5$, $\theta = 135°$) and C ($r = 5$, $\theta = 180°$) (see Fig. 25). The time of measurement goes from $t = 0$ to $t = 10$. The measured values of pressure are compared with the analytical values, given in [25].

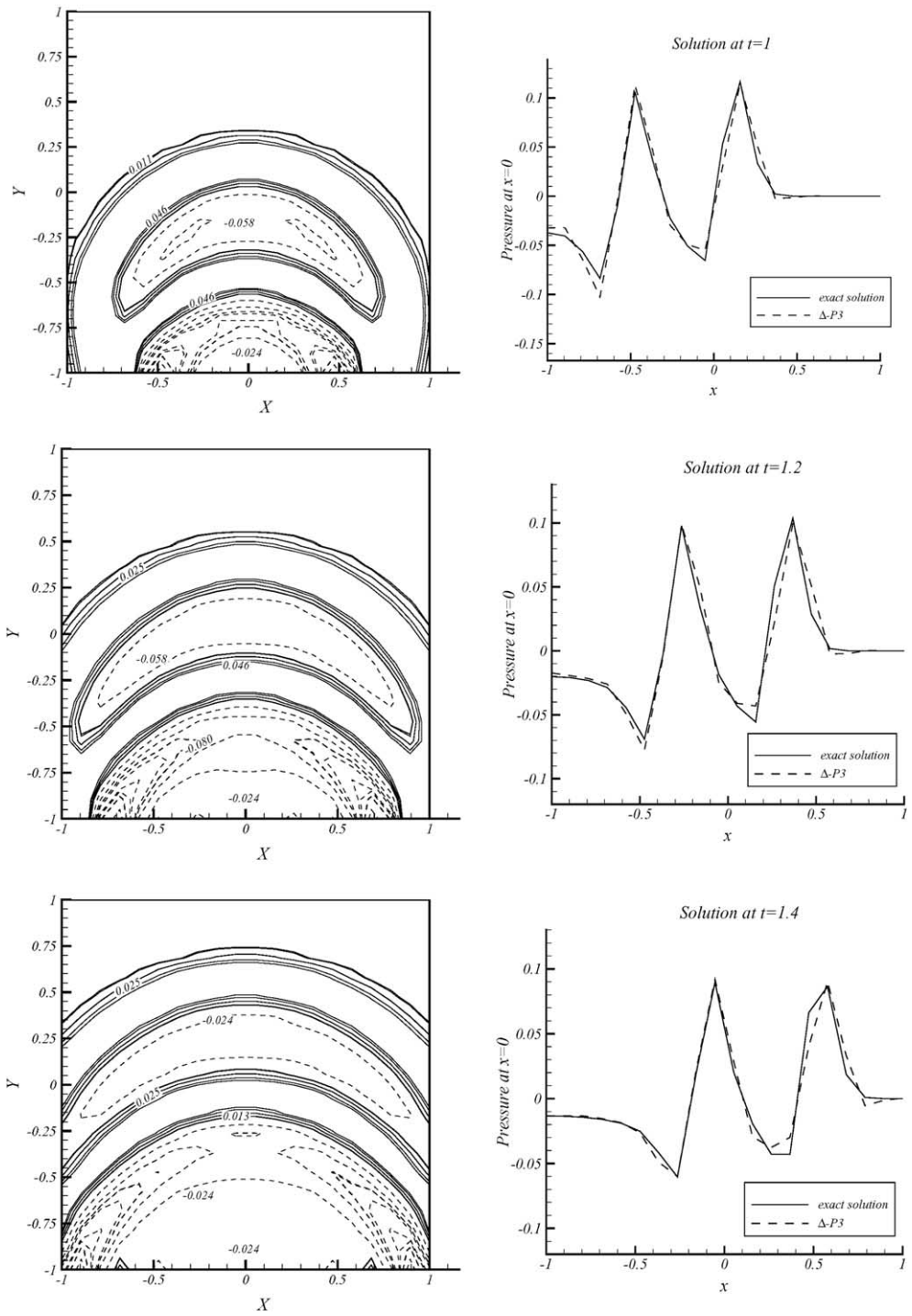

Fig. 17. Acoustic pulse reflected from a wall: Δ-P3 scheme. CFL = 0.5, 20 × 20 Cartesian mesh.

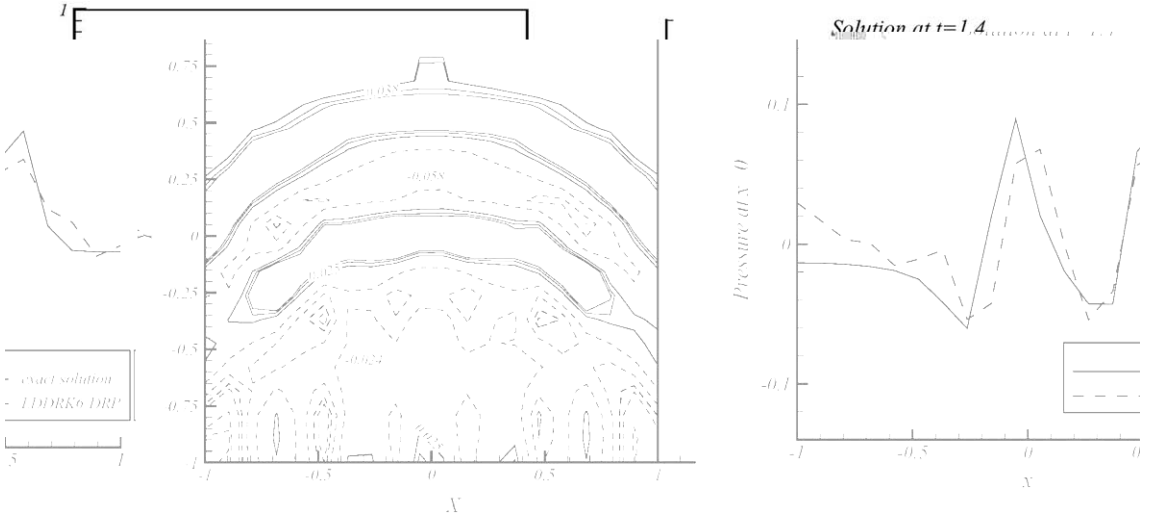

Fig. 18. Acoustic pulse reflected from a wall: LDDRK6–DRP scheme. CFL = 0.5, 20 × 20 Cartesian mesh.

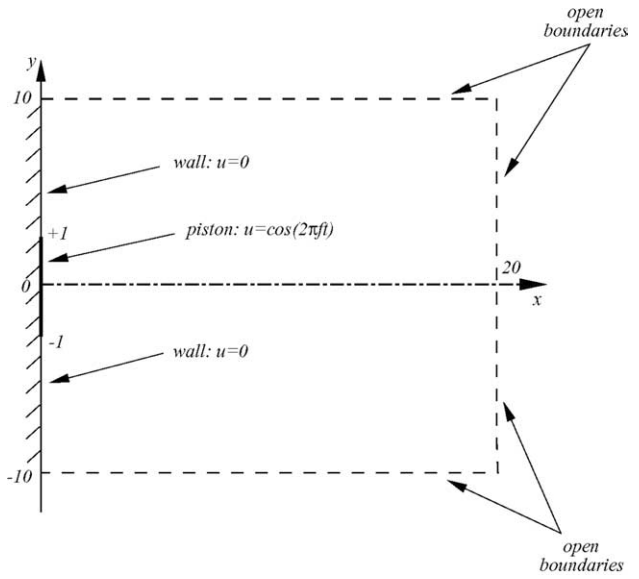

Fig. 19. Linear acoustics: geometry of the two-dimensional piston problem [10].

We obtain the solution to this problem by solving the linearized Euler equations in polar coordinates:

$$\frac{\partial}{\partial t}\begin{bmatrix} p \\ u_r \\ u_\theta \end{bmatrix} + \frac{\partial}{\partial r}\begin{bmatrix} u_r \\ p \\ 0 \end{bmatrix} + \frac{1}{r}\frac{\partial}{\partial \theta}\begin{bmatrix} u_\theta \\ 0 \\ p \end{bmatrix} = -\frac{1}{r}\begin{bmatrix} 0 \\ 0 \\ u_r \end{bmatrix}. \tag{32}$$

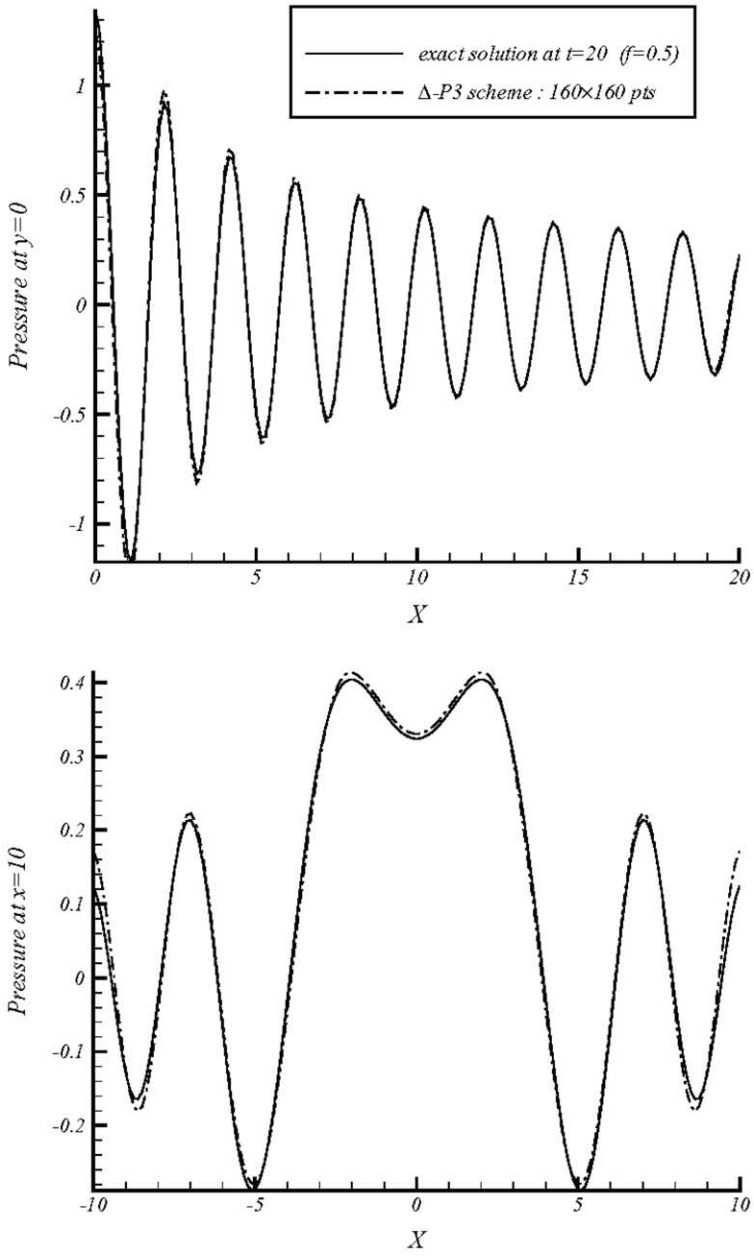

Fig. 20. Piston problem: axial (top) and lateral pressure distribution at $x = 10$ (bottom) for the Δ-P3 scheme: CFL = 0.50, 160×160 grid points, $t = 20$, $f = 0.5$.

The initial solution is as follows:

$$\begin{cases} u_r(r,\theta) = u_\theta(r,\theta) = 0, \\ p(r,\theta) = \exp\left\{-17 \times [(r\cos\theta - 4)^2 + (r\sin\theta)^2]\right\}. \end{cases} \tag{33}$$

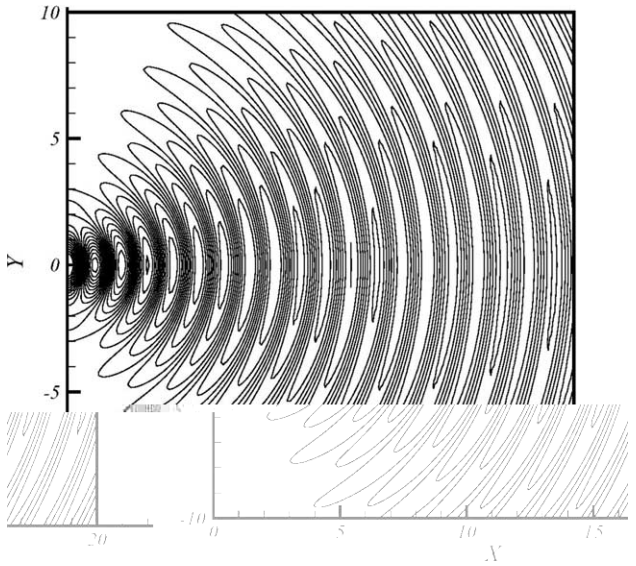

Fig. 21. Pressure contour plots of piston problem at $t = 20$ for $f = 0.5$. Δ-P3 scheme (160×160 grid points, CFL = 0.5).

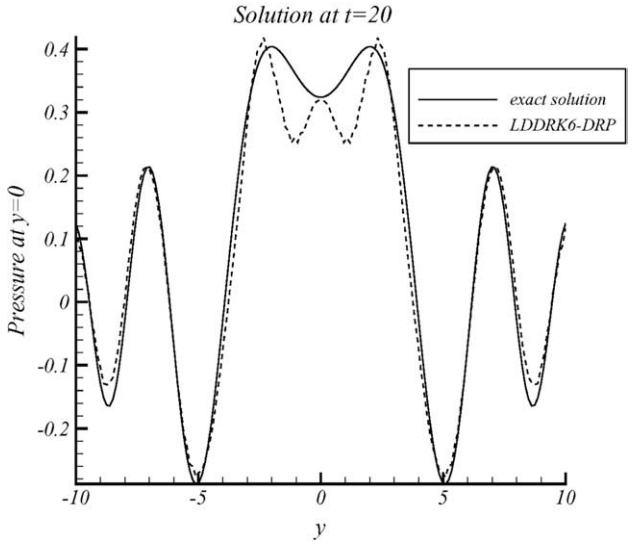

Fig. 22. Piston problem: lateral pressure distribution at $x = 10$ for the LDDRK6–DRP scheme: CFL = 0.50, 160×160 grid points, $t = 20$, $f = 0.5$.

The derivation of this relation initializes the derivative variables. The contribution of the source term, u_r/r, is taken into account by introducing the generic term, U/r, in the wave model, (17), to give

$$\begin{cases} \psi_1 \equiv -P_\tau + \frac{1}{2}\left(U_r + \frac{1}{r_i}V_\theta + \frac{U}{r_i}\right), \quad \psi_4 \equiv -P_n + \frac{1}{2}\left(U_r + \frac{1}{r_i}V_\theta + \frac{U}{r_i}\right), \\ \psi_2 \equiv P_n + \frac{1}{2}\left(U_r + \frac{1}{r_i}V_\theta + \frac{U}{r_i}\right), \quad \psi_3 \equiv P_\tau + \frac{1}{2}\left(U_r + \frac{1}{r_i}V_\theta + \frac{U}{r_i}\right). \end{cases} \tag{34}$$

Then, the algorithm producing the Δ-P3 scheme remains the same one as that described in Section 3.4.

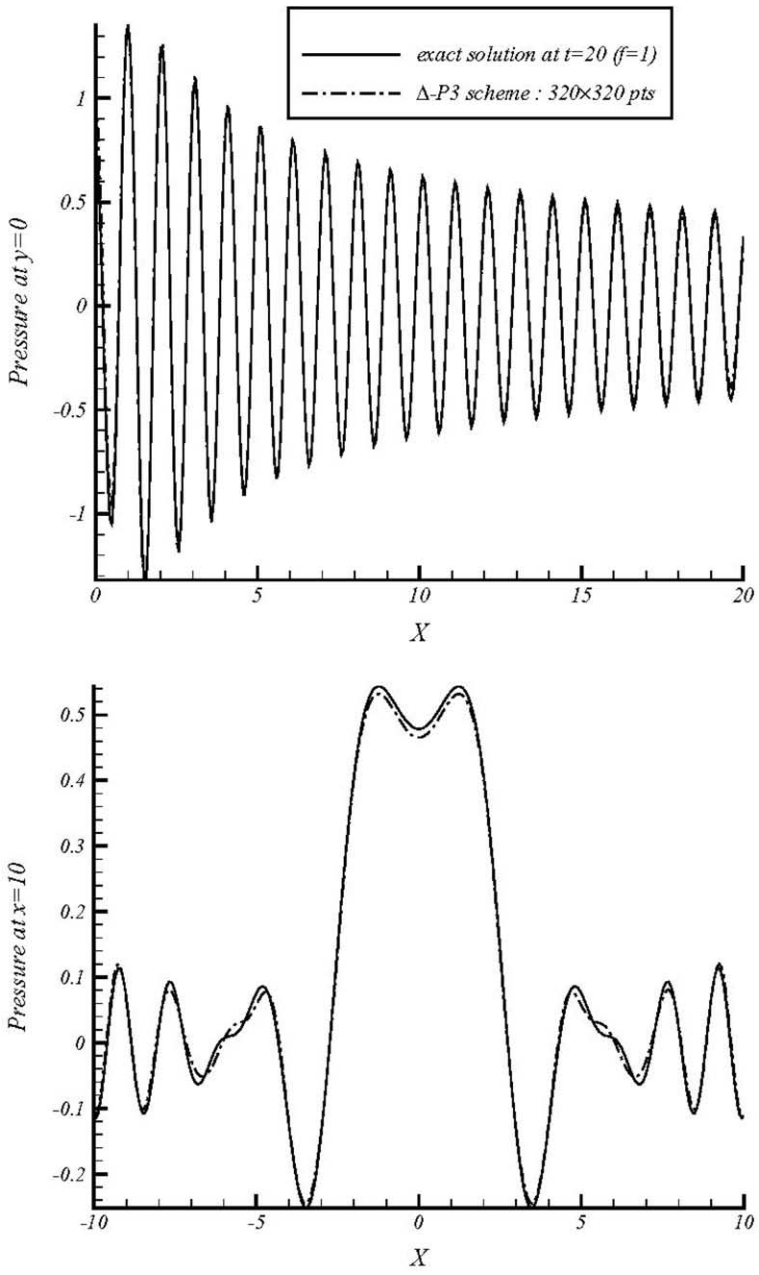

Fig. 23. Piston problem: axial (top) and lateral pressure distribution at $x = 10$ (bottom) for the Δ-P3 scheme: CFL = 0.50, 320×320 grid points, $t = 20$, $f = 1$.

For the numerical simulations, the distance of the far-field boundary from the cylinder is $r_{\max} = 3\pi$. The problem is symmetric about the x-axis, thus, only the solution in the upper half x–y domain, is computed. The grid resolution is imposed such as $\Delta r = \Delta\theta \equiv h$. The Courant number is always defined by $\Delta t/h$ and the

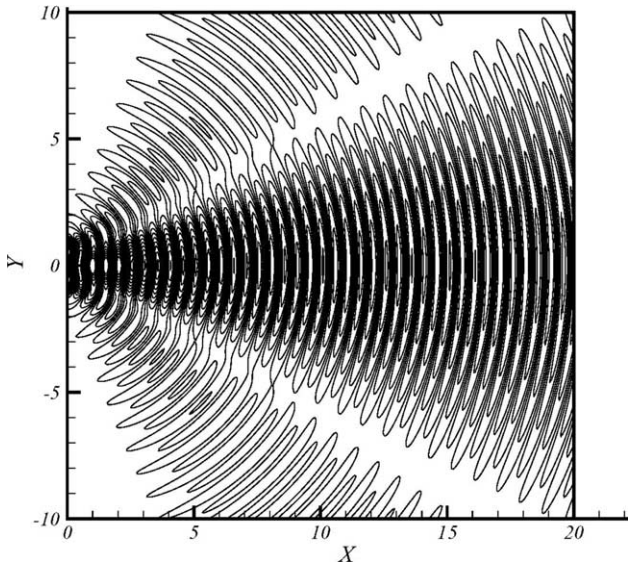

Fig. 24. Pressure contour plots of piston problem at $t = 20$ for $f = 1$. Δ-P3 scheme (320×320 grid points, CFL = 0.5).

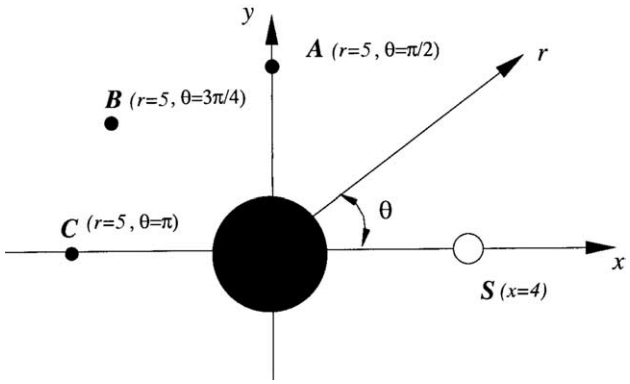

Fig. 25. Geometry of acoustic scattering from a cylinder.

formulae such as (24) and (25), can be preserved. 400 radial grid points and 134 azimuthal grid points are employed for all simulations.

Three boundary conditions are used for this problem: a wall condition on the cylinder ($r = 0.5$), according to the formula (1); an acoustic radiation condition in the far-field ($r = r_{max}$), following the procedure defined by Fig. 14; a symmetry condition at the azimuthal boundaries $\theta = 0$ and $\theta = \pi$, by using the formula (2). For the DRP scheme, the boundary procedures defined in the preceding section remain unchanged. A low CFL number is employed in all simulations (CFL = 0.25) in order to avoid any numerical problem at the points of stagnation ($r = 0.5$, $\theta = 0$ and $\theta = \pi$), situated at the same time on the wall and the line of symmetry.

Fig. 26 shows the temporal evolutions of the pressure at the points A, B, C. As one can note it, the numerical solution is very close to the exact solution, except the solution at the point A which requires more

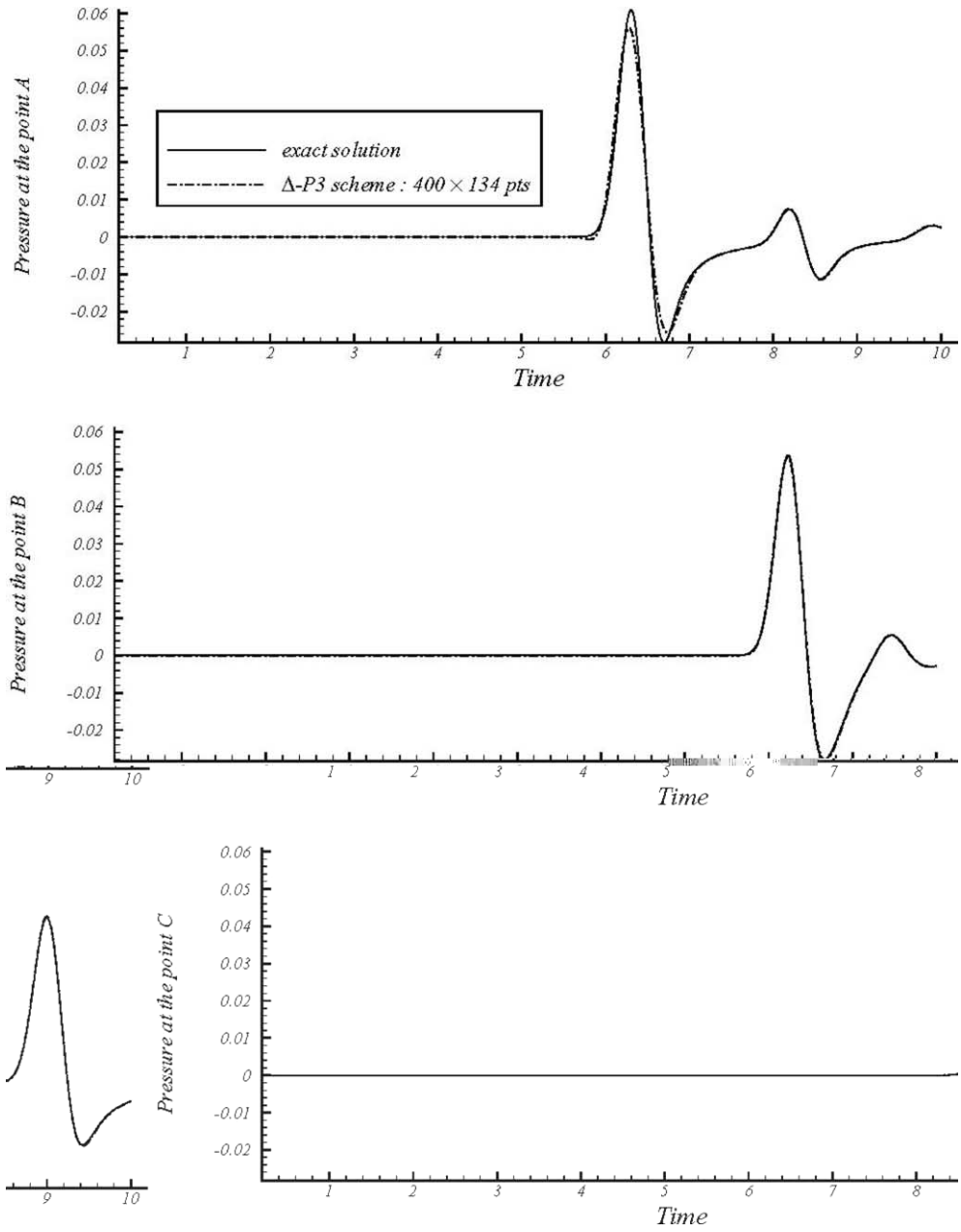

Fig. 26. Acoustic scattering from a cylinder. Δ-P3 scheme: time history of pressure fluctuations at points A, B, C. CFL = 0.25. p_{max} at point A = 0.0563 (400 × 134 grid points).

grid points. Fig. 27 shows contour plots of these results with $t = 1.2$, 3.8, 5 and 6.2 (dashed lines represent negative values of the pressure). As show it the results obtained for $t = 6.2$, there are three wave fronts. That which is furthest away from the cylinder is the wave front created by the initial conditions. The following is

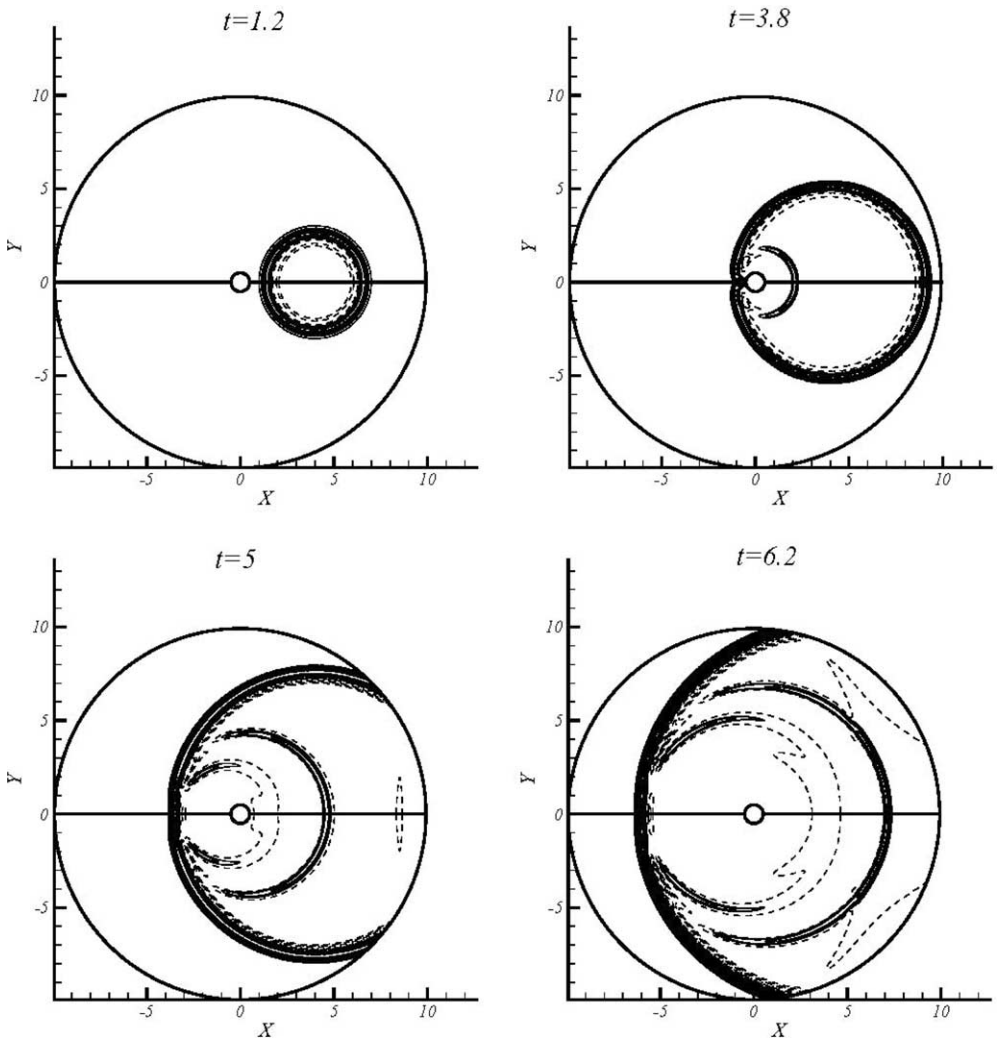

Fig. 27. Acoustic scattering from a cylinder. Δ-P3 scheme: pressure pulse contours for the acoustic scattering problem. 400×134 grid points, CFL = 0.25.

the wave reflected starting from the right surface of the cylinder, facing directly on the initial pulse. The wave front nearest to the cylinder is generated when the two parts of the initial wave front, generated by the cylinder, ran up and amalgamated on the left surface of the cylinder. This posterior wave front is weaker than the two others.

The fact that no artificial reflection occurs starting from the outer boundary, indicates that the condition of far-field non-reflecting boundary is effective to transmit the waves. Moreover, there are no spurious oscillations close to the wall: the wall condition seems to function successfully. On the other hand, Fig. 28 shows the dispersive nature of the LDDRK6–DRP scheme at the point A.

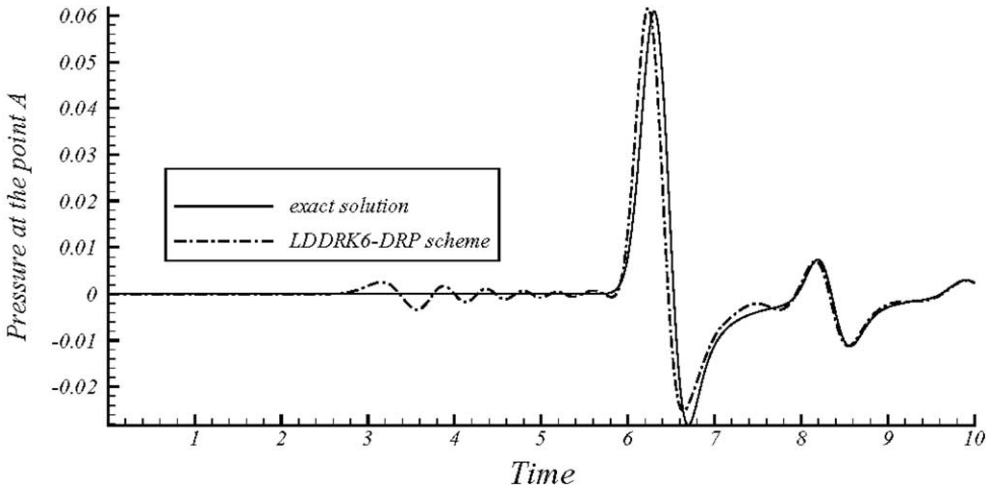

Fig. 28. Acoustic scattering from a cylinder. LDDRK6–DRP scheme: time history of pressure fluctuations at point A ($r = 5$, $\theta = 90°$), CFL = 0.25. (400×134 grid points).

5. Summary and concluding remarks

The principal idea of this paper is that a time-marching scheme of high-order can accurately reproduce the multi-dimensional wave propagation for a linear problem, if the stencil defined for the dicretization process is strongly compact and upwinded correctly.

A convenient manner to build such a scheme is to divide the process of discretization into three parts:

- a reconstruction stage
- a decomposition stage
- an evolution stage

In the reconstruction stage, the function and its derivatives are used to define a local spatial interpolator in each step of time. This stage contributes to generate a high-order compact scheme.

In the decomposition stage, the time-derivatives are broken up into simple waves, according to the ideas of Roe [4]. For the acoustic equations, four simple acoustic waves being propagated with 90° to each other, are selected while being based on physical arguments and numerical simulations. These waves are characterized by a ''propagation angle'', θ, which is selected with the value $\pi/4$ for the acoustic equations. Then, the wave strengths are calculated. This decomposition allows a suitable upwinding of the discrete stencil by choosing the waves which move towards a given discrete point. This upwinding supports a natural treatment of the boundary conditions by distinguishing waves entering and outgoing from the calculation domain. In this way, conditions of radiation and wall boundary were proposed in order to prevent the appearance of spurious numerical short wavelengths.

In the evolution stage, the function and its derivatives are brought up to date according to a procedure of Cauchy–Kovaleskaya. This stage is important because the mechanism of propagation of wave involves a coupling between space and time.

Based on a Fourier analysis, we showed that resulting scheme produces a low level of dissipative and dispersive errors by using 15 cells-per-wavelength.

The method thus generated was studied and validated on problems concerning the propagation of the sound in a uniform medium at rest. The advantages of our approach are then the following:

- A compact upwind scheme seems to be the natural way to do numerical convection since it generates a very low dispersive error, while maintaining the amplitude error on a reasonable level.
- To break up the algorithm into three sub-problems gives more facilities to optimize and adapt the resulting scheme according to the problem considered.
- The space discretization is really multi-dimensional since the linear four-wave pattern used in the decomposition stage is free of the grid orientation.
- The effectiveness of the non-reflecting boundary conditions is obvious, at least in the test cases considered. Moreover, the scheme does not change close to a boundary: there is no need to introduce ghost points.
- For the generated scheme, the availability of continuous functions inside each mesh (local space interpolator, $\tilde{\varphi}(x,y)$) and freedom to choose these last, allow the introduction of additional physical terms and to satisfy special conditions (interpolation or extrapolation of the solution, extension to curvilinear meshes, etc.).
- While keeping the same structure, the algorithm can be improved by adding more information in each cell. For example, adding second derivatives as unknowns, makes it possible to generate a compact scheme of fifth-order.
- Despite its algebraic complexity, a compact upwind Hermitian scheme is competing with "state of the art" numerical methods, simpler formally.

This last advantage justifies the efforts carried out to generate a specific algorithm for the multi-dimensional and linear wave propagation. However, one can note that the numerical method requires a careful specification of an initial condition for the derivative because its effect on stability is not clearly identified. This disadvantage is similar with that of multi-step time-integration schemes, which always require a separate method to start calculation.

In a future paper, this approach will be extended to the discretization of the aeroacoustic equations.

Acknowledgement

The author wishes to thanks with recognition, Dr. G.B. Deng (Ecole Centrale de Nantes, France) to have provided a technical support essential to this work.

Appendix A. Accurate component–spurious component

Let us consider the scalar advection equation:

$$u_t + a u_x = 0 \quad (a \equiv Cte > 0). \tag{A1}$$

Let us suppose that we discretize (A1) by using the Δ-P3 scheme. We now have to consider the following system of E.D.P:

$$U_t + A U_x = 0 \tag{A2}$$

with $U \equiv [u, r]^t$, $A \equiv \mathrm{diag}(a,a)$,$r \equiv \Delta x \times u_x$. By applying the Fourier transform of (A2), $U(x,t) = \hat{U}(t) \times e^{ikx}$, it is easy to obtain

$$\frac{\mathrm{d}\hat{U}(t)}{\mathrm{d}t} + \mathrm{j}kA\hat{U}(t) = 0 \quad (\mathrm{j}^2 = -1). \tag{A3}$$

Hence, we can integrate (A3) between $t = 0$ and $t = t_{n+1} \equiv (n+1)\Delta t$ to produce the following result:

$$\hat{U}(t_{n+1}) = \hat{u}(0) \times \mathrm{e}^{-\mathrm{j}(n+1)\beta v} \times \begin{bmatrix} 1 \\ \mathrm{j}\beta \end{bmatrix}. \tag{A4}$$

This relation can be written in an equivalent way as

$$\begin{cases} \hat{u}^{n+1} = \mathrm{e}^{-\mathrm{j}v\beta}\hat{u}^n, \\ \hat{r}^{n+1} = \mathrm{e}^{-\mathrm{j}v\beta}\hat{r}^n. \end{cases} \tag{A5}$$

This relation indicates that the function and its derivative are convected in the same way and that the exact amplification factor of (A2) is given by $\mathrm{e}^{-\mathrm{j}v\beta}$.

Denoting, respectively, by $v_a(\beta, v)$ and $\lambda_a(\beta, v)$, the eigeinvector and amplification factor (eigenvalue) of (A2), we can deduce with (A4) the following results:

$$v_a(\beta, v) \equiv \begin{bmatrix} 1 \\ \mathrm{j}\beta \end{bmatrix}, \quad \lambda_a(\beta, v) \equiv \mathrm{e}^{-\mathrm{j}v\beta}.$$

Now, a discrete Fourier transform of the resulting algebraic system produced by the Δ-P3 scheme, gives the following result:

$$\hat{U}^{n+1} = G(\beta, v) \times \hat{U}^n \tag{A6}$$

with $G(\beta, v)$, the amplification matrix, given in Section 2.2.

The eigenvalues and eigeinvectors of $G(\beta, v)$ can be calculated using the Maple symbolic mathematical computer package. By defining the first eigenvalue, $\lambda_1(\beta, v)$, as the approximation of $\lambda_a(\beta, v)$, the second eigenvalue, $\lambda_2(\beta, v)$, which has no counterpart in the differential system (A2), is then referred to as the "spurious" eigenvalue. By defining $\Lambda(\beta, v)$ as the diagonal matrix with the eigenvalues $\lambda_p(\beta, v)$ $(p = 1, 2)$ on the diagonal and V, the matrix with the right eigenvectors $v_p(\beta, v)$ as columns, (A6) can be diagonalized; the system (A6) is then decoupled by the transformation of $\hat{U}$ into the characteristics variables: $\hat{W} \equiv [\hat{w}_1, \hat{w}_2]^t$ defined by

$$\hat{W} \equiv V^{-1}\hat{U} \tag{A7}$$

with the inverse transformation

$$\hat{U} = V \times \hat{W} = \sum_{p=1}^{2} \hat{w}_p v_p. \tag{A8}$$

The decoupled system is then given by

$$\hat{W}^{n+1} = \Lambda\hat{W}^n. \tag{A9}$$

Therefore, by considering (A8) and (A9), we can deduce the relation:

$$\hat{U}^{n+1} = \sum_{p=1}^{2} \lambda_p^{n+1}\hat{w}_p^0 \times v_p \quad (\hat{w}_p^0 \equiv \hat{w}_p(t=0)). \tag{A10}$$

This relation must be compared with the exact one, (A4). The term $\lambda_1^{n+1}v_1$ represents the approximation of $\lambda_a^{n+1}v_a$ since $\lambda_1^{n+1}v_1 \to \lambda_a^{n+1}v_a$ as $\beta \to 0$: this is the accurate component of the solution. Consequently, the remaining term $\lambda_2^{n+1}v_2$, which has no equivalent in (A4), is referred to as the "spurious" component.

Hence, by using an inverse Fourier transform, the numerical solution discretizing (A2) with the help of the Δ-P3 scheme, will be the following:

$$U_i^{n+1} = \sum_{p=1}^{2} \lambda_p^{n+1} \hat{w}_p^0 \times e^{ikx_i} \times v_p. \tag{A11}$$

Then, the accurate component of U_i^{n+1} is defined by

$$\lambda_1^{n+1} \hat{w}_1^0 \times v_1 \times e^{i\frac{\beta}{\Delta x} x_i}$$

and may be calculated for a given wave number (β known) and a given initial solution of (A1) ($\hat{w}_1^0$ known), at each time step. Such a term represents the convection by the numerical scheme of the numerical variable and its derivative, at the speed λ_1.

On the other hand, the spurious component at $t = t_{n+1}$ is defined by

$$\lambda_2^{n+1} \hat{w}_2^0 \times v_2 \times e^{i\frac{\beta}{\Delta x} x_i}.$$

This term no more represents a convective process. It only represents the numerical error introduced by the discretization of the second equation of (A2) into the first equation and reciprocally. This term is due to the numerical coupling between the function and its derivative into the algebraic system.

If $|\lambda_2| < 1$ or if $\hat{w}_2^0 \equiv 0$, then this component is quickly damped or even does not exist and therefore has no influence on the overall accuracy of the Δ-P3 scheme.

References

[1] P. Garabedian, Partial Differential Equations, Wiley, New York, 1964.
[2] P.L. Roe, Linear bicharacteristic schemes without dissipation, ICASE Report 94-65, 1994.
[3] P.L. Roe, Local reduction of certain wave operators to one-dimensional form, ICASE Report 94-66, 1994.
[4] P.L. Roe, Discrete models for the numerical analysis of time-dependent multi-dimensional gas dynamics, J. Comput. Phys. 63 (1986) 458–476.
[5] C.K.W. Tam, Advances in numerical boundary conditions for computational aeroacoustics, AIAA Paper-97-1774, 1997.
[6] S.K. Lele, Compact finite-difference schemes with spectral-like resolution, J. Comput. Phys. 103 (1992) 16–42.
[7] C.K.W. Tam, K.A. Kurbatskii, J. Fang, Numerical boundary conditions for computational aeroacoustics benchmark problems, in: C.K.W. Tam, J.C. Hardin (Eds.), Proceedings of the Second Computational Aeroacoustics Workshop on Benchmark Problems, 1997.
[8] P.L. Roe, C. Kim, Accurate schemes for advection and aeroacoustics, AIAA Paper-97-32412, 1997.
[9] C.K.W. Tam, J.C. Hardin, J.R. Ristorcelli (Eds.), Workshop on Benchmark Problems in Computational Aeroacoustics, NASA Conference Paper 3300, 1995.
[10] A.P. Dowling, J.E. Ffowcs-Williams, Sound and Source of Sound, Wiley, New York, 1983.
[11] C.K.W. Tam, J.C. Webb, Dispersion–relation-preserving finite difference schemes for computational acoustics, J. Comput. Phys. 107 (1993) 262–281.
[12] F.Q. Hu, M.Y. Hussaini, J.L. Manthey, Low-dissipation and low-dispersion Runge–Kutta schemes for computational acoustics, J. Comput. Phys. 124 (1996) 177–191.
[13] Z. Haras, S. Ta'asan, Finite-difference schemes for long-time integration, J. Comput. Phys. 114 (1994) 265–279.
[14] D.W. Zing, H. Lomax, H.M. Jurgens, High-accuracy finite-difference scheme for linear wave propagation, SIAM J. Sci. Comput. 17 (1996) 328–346.
[15] R. Hixon, E. Turkel, High-accuracy compact Mc-Cormack-type schemes for computational aeroacoustics, AIAA Paper 98-0365, 1998.
[16] Z.J. Wang, R.F. Chen, Optimized weighted essentially non-oscillatory schemes for linear waves with discontinuity, J. Comput. Phys. 174 (2001) 381–404.
[17] C. Kim, P.L. Roe, J.P. Thomas, Accurate schemes for advection and aeroacoustics, AIAA Paper 97-2091, 1997.
[18] S.C. Chang, The method of space–time conservation element and solution element – a new approach for solving the Navier–Stokes and Euler equations, J. Comput. Phys. 119 (1995) 295–324.

[19] H.L. Atkins, C. Shu, Continued development of the discontinuous Galerkin method for computational aeroacoustic applications, AIAA Paper 97-1581, 1997.
[20] M. Zhuang, R.F. Chen, On study of the optimised upwind dispersion–relation-preserving finite-difference schemes in computational aeroacoustics, AIAA Paper 97-1607, 1997.
[21] B. Van-Leer, Towards the ultimate conservative difference scheme, IV. A new approach to numerical convection, J. Comput. Phys. 23 (1977).
[22] J. Qiu, C.-W. Shu, Hermite WENO schemes and their applications as limiters for Runge–Kutta discontinuous Galerkin method: one dimensional case, J. Comput. Phys. 193 (2003) 115–135.
[23] J.W. Goodrich, A. Dyson, Automated approach to very high-order aeroacoustic computations, AIAA J 39 (3) (2001) 396–406.
[24] J.W. Goodrich, A comparison of numerical methods for computational aeroacoustics, AIAA Paper 99-1943, 1999.
[25] C.K.W. Tam, J.C. Hardin (Eds.), Second Computational Aeroacoustics Workshop on Benchmark Problems, NASA Conference Paper-3352, June 1997.